1-1-2016

Toward Magnetic Resonance Only Treatment Planning: Distortion Mitigation And Image-Guided Radiation Therapy Validation

Ryan Glen Price
Wayne State University,

TOWARD MAGNETIC RESONANCE ONLY TREATMENT PLANNING: DISTORTION MITIGATION AND IMAGE-GUIDED RADIATION THERAPY VALIDATION

by

RYAN GLEN PRICE

DISSERTATION

Submitted to the Graduate School

of Wayne State University,

Detroit, Michigan

in partial fulfillment of the requirements

for the degree of

DOCTOR OF PHILOSOPHY

2016

MAJOR: MEDICAL PHYSICS

Approved By:

_____

Advisor Date

_____

_____

_____

_____

DEDICATION

To my dad, mom, and sister for their never ending encouragement.

To the many friends who have always pushed me to do better.

To my wife, Tovi, for the constant sacrifice, support, and love she has given throughout this entire journey, and for teaching me by example how to live a life in service of others.

ACKNOWLEDGEMENTS

I would like to thank my dissertation committee: Dr. Indrin J. Chetty, Dr. James Balter, Dr. Hualiang Zhong, Dr. Jay Burmeister, and in particular my advisor Dr. Carri Glide-Hurst for their continued support and constructive criticism throughout this process. I would also like to thank the rest of the MR-SIM research group: Dr. Josh Kim, Dr. Weili Zheng, and David To for the many insightful discussions and late nights worked on my behalf, as well Eric Morris for his enthusiasm to be involved, David Hearshen and Mo Kadbi for offering their expertise, and Robert Knight for the many hours spent on the planning and building phases of the distortion phantom. Henry Ford Health System holds research agreements with Philips Healthcare. Research sponsored in part by an HFHS Internal Mentored Grant (C. Glide-Hurst), NIH R01CA204189, and NIH R01EB016079.

PREFACE

Note to the reader:

Chapters 2-4 of this dissertation were originally written individually for publication in peer reviewed scientific journals, and while much has been added to tie the chapters together as a single cohesive document, they were originally intended to stand-alone. At the time of submission, both Chapter 2 and 4 have been accepted for publication. Chapter 2 was originally published in Medical Physics (2015) under the title “Technical Note: Characterization and correction of gradient nonlinearity induced distortion on a 1.0 T open bore MR-SIM”. Chapter 4 was originally published in the International Journal of Radiation Oncology, Biology, and Physics under the title “Image Guided Radiation Therapy Using Synthetic Computed Tomography Images in Brain Cancer”.

TABLE OF CONTENTS

LIST OF TABLES

LIST OF FIGURES

LIST OF ABBREVIATIONS

OAR ..... Organ at Risk

CT-SIM ..... Computed Tomography Simulation

CT ..... Computed Tomography

RTP ..... Radiotherapy Treatment Planning

GTV ..... Gross Tumor Volume

PTV ..... Planning Target Volume

MRI ..... Magnetic Resonance Imaging

MR ..... Magnetic Resonance

EUD ..... Equivalent Uniform Dose

IMRT ..... Intensity Modulated Radiation Therapy

MR-SIM ..... Magnetic Resonance Simulation

DRR ..... Digitally Reconstructed Radiograph

SynCT ..... Synthetic Computed Tomography

IGRT ..... Image Guided Radiation Therapy

FOV ..... Field of View

GNL ..... Gradient Non-Linearity

A-P ..... Anterior-Posterior

GE ..... Gradient Echo

S-I ..... Superior-Inferior

TE ..... Echo Time

SVD ..... Singular Value Decomposition

PTV ..... Planning Target Volume

L-R ..... Left to Right

RT ..... Radiation Therapy

TSE ..... Turbo Spin Echo

UTE ..... Ultra-fast Echo Time

FFE ..... Fast Field Echo

FLAIR ..... Fluid Attenuated Inversion Recovery

GMM ..... Gaussian Mixture Model

CSF ..... Cerebrospinal Fluid

MAE ..... Mean Absolute Error

NMI ..... Normalized Mutual Information

HU ..... Hounsfield Units

TR ..... Recovery Time

TI ..... Inversion Time

DRR ..... Digitally Reconstructed Radiograph

CHAPTER 1 "INTRODUCTION"

Motivation for Magnetic Resonance Imaging in Radiation Treatment Planning

Linear accelerators have become the workhorse for delivery of radiation in a radiation oncology setting. Traditionally, radiation was delivered using simple geometric beam arrangements to ensure uniform dose coverage of the target. This resulted in large amounts of radiation being delivered to the surrounding healthy tissue, or organs-at-risk (OARs). Technological improvements, such as the development of multi-leaf collimators, have led to the development of techniques for delivering radiation that conforms closely to the tumor while sparing nearby OARs. (e.g. intensity modulated radiation therapy (IMRT)). However, the delivery of conformal dose distributions is dependent on the ability to accurately localize the position of the target as well as OARs for treatment planning, which necessitates highly accurate imaging methods that can clearly distinguish the tumor from nearby OARs. The gold standard for acquiring patient images that will be used to create a customized treatment plan for the patient is computed tomography simulation (CT-SIM), where a computed tomography (CT) image of the patient is collected prior to the treatment day with the patient immobilized and positioned as they will be during treatment delivery. The radiation oncologist then delineates the tumor volume and OARs on the CT image, which are used to generate an optimal dose distribution for the patient.

CT is the standard imaging modality used in radiotherapy treatment planning (RTP) due to its excellent geometric accuracy and straightforward conversion from image intensity values to electron density values of the object. The latter feature allows for the CT intensity values to be easily used for heterogeneity corrections during

treatment planning dose calculations.[1]

However, the electron density, and therefore image intensity, of many soft tissues are very similar, making it challenging to distinguish between these tissues on a CT image. While all steps in the treatment planning and delivery process introduce uncertainty in patient treatment, the delineation of the gross tumor volume (GTV) on CT images introduces some of the greatest uncertainty in the entire RTP workflow.[2-6] In one study involving 6 physicians contouring on CT images for 3 prostate cases, Cazzaniga *et al*. reported an inter-observer target delineation uncertainty of 36%.[4] For RTP in the brain, Weltens *et al*. demonstrated large inter-observer variability in GTV delineation with nearly a 3-fold difference between the largest and smallest defined contours.[5] Similarly, Valley *et al*. noted more than an eight-fold difference between smallest and largest defined planning target volumes (PTVs) in the delineation of head and neck carcinomas.[6]

To reduce this variability and improve the ability to visualize many tumors, magnetic resonance imaging (MRI), with its excellent soft tissue contrast, is often used as an adjunct to CT for target delineation.[7, 8] MRI relies on a complex set of imaging parameters that can drastically change the resultant image contrast. This enables much more flexibility than CT in differentiating neighboring tissues to allow for accurate characterization of the extent of the tumor, even when surrounded by soft tissue with similar electron density as shown in Figure 1. When MRI is used in radiation therapy, MR images are typically employed to contour the target and OARs, which are then propagated to the CT image via image registration. The CT is then used for treatment planning and dose calculations. The integration of MRI in RTP has been shown to

significantly reduce inter-observer and intra-observer delineation variability for many disease sites.[9-13] In one study, the use of MR/CT resulted the reduction of the standard deviation of GTV delineation for nasopharynx cancer of up to 4.4mm (dependent on location of tumor).[10] Jolicoeur *et al*. also showed a significant reduction in inter-observer variability in surgical bed delineation for breast interstitial brachytherapy when fusing MRI with CT. For MRI there was no statistically significant inter-observer variability between delineated volumes, while the variability was highly significant when CT alone was used.[11]

The use of MRI can also be crucial in determining the extent of the tumor during treatment planning. In a nasopharyngeal carcinoma image comparison study by Emami *et al*, tumor infiltration of the surrounding tissue which was missed on the CT was noted on many patient MR images, which resulted in a 74% increase in target volume when using MRI.[14] While in a similar study utilizing scans from 258 patients, Chung *et al* noted over 40% of patients had infiltration that was not detected by the CT scan alone.[15] MRI has been proven to be valuable in determining boundaries between the target and OARs(e.g. between the prostate and the bordering bladder and rectal wall[16, 17]) and in assessment of the infiltration of the anus and/or uterus for rectal cancer.[18, 19]

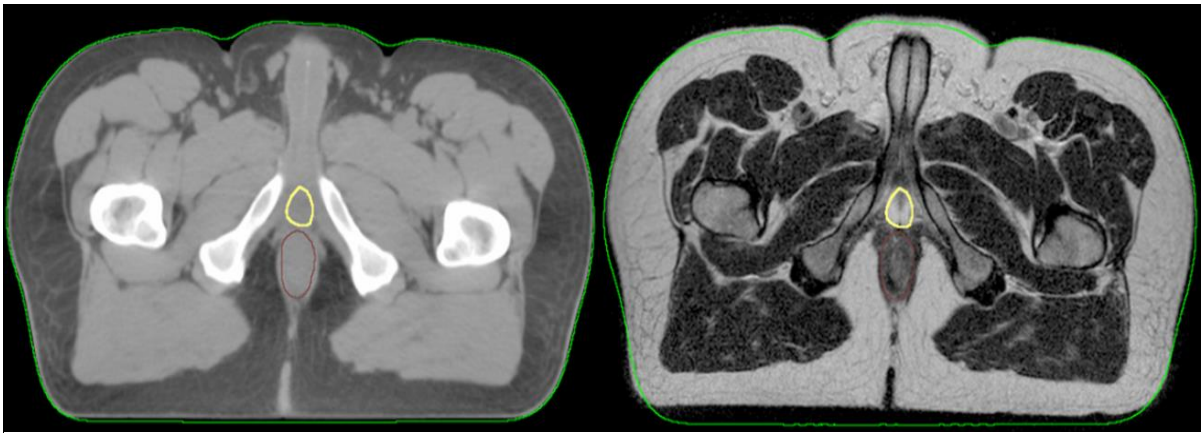

Figure 1: MRI (right) provides superior soft tissue contrast to CT(left), and can be useful for improved delineation of the target and OARs.

Use of MRI as an adjunct to CT for delineation has demonstrated significant benefits for dosimetry and overall treatment outcomes. MRI-delineated prostate plans have been shown to reduce equivalent uniform dose (EUD) to the rectal wall by 3.6Gy, allowing for dose escalation to the PTV while maintaining the same EUD to the rectal wall as in CT-delineated plans.[20] Similarly, an MRI-assisted dose escalation and dose volume adaptation study focusing on locally advanced cervical cancer described the potential benefits of MRI on overall treatment outcomes, where patients undergoing MR-assisted dose volume escalation showed up to a 20% increase in local control and overall survival while decreasing gastrointestinal and urinary late morbidity.[21]

Rationale for MR-Only Simulation

While MRI has demonstrated considerable benefits when used as an adjunct to CT for treatment planning, the co-registration process between imaging modalities can introduce additional systematic uncertainties.[22-27] Ulin *et al*. conducted a multi-institutional study that benchmarked the accuracy of cranial MR-CT registration by distributing the same image set to 45 institutions and allowing each of them to register the images using those registration methods that were consistent with the standard clinical practice of each individual institution. On average, there was ~2mm of uncertainty introduced from the known target position (1 standard deviation).[23] Similar studies utilizing both mutual information (MI) and landmark matching to measure the co-registration uncertainties for prostate reported an average uncertainty of 2-3mm.[24-26] These systematic errors introduced during multiple modality image registration can be detrimental to the accuracy of the treatment plan by shifting high dose regions away from the target[27], which could compromise tumor control for when using conformal

margins.

MR simulation (MR-SIM) platforms have recently been developed that can potentially reduce some of the registration uncertainties involved in integrating MRI in the RTP workflow.[28, 29] In order to integrate MRI into RTP, several logistical issues need to be addressed that necessitate some key differences between these MR-SIM platforms and traditional MR scanners. First, MR scanners utilize curved table tops, which are inappropriate for use in treatment planning simulation. Therefore, specially designed flat table top inserts must be installed in order to provide a surrogate for the treatment table. The couch tops may take the form of couch replacements or overlays, but they all must be able to be indexed for repeatable set-up of patients and corresponding immobilization devices between the MR-SIM and the treatment room. Second, immobilization devices provide their own challenge in that several immobilization devices are incompatible with the MR system. Therefore, MR-compatible immobilization devices must be introduced that can be used for both simulation and treatment. Additionally, traditional MR bore sizes are too small to accommodate these immobilization devices used in radiotherapy. As a result, larger bore sizes and open bore geometries have been developed that can accommodate bulkier immobilization equipment and larger patients. Next, while many MR systems are equipped with a single integrated laser, reproducible set-up requires the use of multiple external lasers to allow marking of the patient to indicate both translational and rotational alignment along and about all three axes. To satisfy these requirements, MR-compatible external laser marking systems are used as a proxy for the laser systems in the treatment room. Finally, dedicated radiation therapy scanning protocols that meet the needs of RTP

have been developed. It is also important for RTP protocols to include a high readout bandwidth for minimization of distortions, contiguous slices with a minimal slice thickness for optimal DRR image quality, and increased uniformity for accurate registration and segmentation.[30] Furthermore, ultra-fast imaging techniques have also been implemented to support the minimization of patient and organ motion during acquisition, while alternatively, 4D-MRI and cine acquisition modes have been used to instead measure this motion.

While imaging patients for RTP in the treatment position using the same immobilization devices is likely to improve the co-registration accuracy, this uncertainty could be eliminated via an MR-only treatment planning workflow. Implementing MR-only RTP would exploit the benefits of MRI for target and OAR delineation by avoiding the systematic uncertainties associated with multi-modality image registration, while increasing clinical efficiency and reducing imaging dose, patient time, and overall imaging costs. For these reasons, many groups have shown interest in developing MR-only RTP.[21, 31-37] In a pilot study, Beavis *et al*. utilized a water phantom and custom RTP imaging sequences and demonstrated that with proper gradient selection within the FOV of the brain (<10cm), no distortions greater than 1mm were found, and thus no corrections were necessary for the MR images.[38] Lee *et al*., tested the practicality of an MR-only approach for prostate cancer and found negligible differences between dose distributions calculated on MR-derived images vs CT. He concluded that since the development of newer sequences that provide higher quality images with decreased geometric distortion, MR-only planning for the prostate could feasibly be implemented within the clinical workflow.[39] Similarly, Kapanen *et al*. performed a quantitative analysis

of the overall geometrical accuracy of MR-only RTP for the prostate, and proposed a set of procedures to support its implementation into the clinic.[32] Dose calculation accuracy has also been investigated for lung RTP, as well as head and neck by Jonsson *et al*., with only small deviations from CT.[40]

The Challenges of MR-SIM Only in Treatment Planning: Statement of Problem

While MR-only treatment planning has shown promise, there are still several well-known challenges that are currently limiting widespread clinical implementation. Firstly, MR images are affected by both patient-induced and system-level geometric distortions that can significantly degrade treatment planning accuracy. While some of these distortions are smaller near magnet isocenter, distortions as high as 23mm have been measured.[41] Accurate geometric fidelity across the entire field of view (FOV) is essential if MR-only RTP is to be implemented.[42, 43] The total distortion is dependent on a variety of factors, and many studies exist that attempt to isolate and correct for each type of distortion. Chang *et al*. conducted a study showing some distortions resulting from static field inhomogeneites could be corrected via a manipulation of the gradients.[44] Some have sought to partially correct gradient non-linearity induced distortions via modeling of the complex fields,[45] while others have utilized post-processing corrections based on direct phantom measurements.[46, 47] Some methods require patient specific corrections[48] which can utilize phase mapping techniques to measure inhomogeneities induced in the B_0 field. While the techniques used for mitigating distortion have improved, construction of wider bore magnets and faster gradients have led to increased distortions due to reduced homogeneity and increased gradient nonlinearity.[49] Much work has also been conducted to develop distortion

phantoms to measure and characterize distortions across large field of views (FOVs).[50-52] However, very few provide sufficiently large FOV coverage, and those that do have been customized to meet the geometric requirements of the specific MR system employed by the institution that developed the phantom. In addition, the availability of comprehensive distortion analysis software is currently limited.

MRI does not inherently provide electron density information, which is necessary for accurate dose calculation using tissue inhomogeneity corrections and digitally reconstructed radiograph (DRR) generation. Many groups have been working toward generating a synthetic CT (synCT),[53-59] which maps intensity values of MR images to estimated electron density values. Groups such as Johansson *et al*. have developed automatic synCT generation based on advanced MR imaging sequences,[56] Andreasen *et al*. demonstrated the use of a multi-patient database to assign HU values,[55] and Sjolund *et al*. used registration and an atlas-based database.[58] While the generation of synCT images can enable dose calculation on an MR-only data set,[54, 60] further study is needed on the implementation of synCTs as the reference datasets for linac-based image-guided radiation therapy (IGRT) to help determine their robustness in an MR-only workflow. Thus, the overarching goal of this work is to address some of the major challenges that exist in implementing MR-only RTP via the following specific aims:

Specific Aims

1) To perform technical characterization of gradient non-linearity induced distortion for large FOVs, including the development and evaluation of a correction scheme, and the quantification of the temporal stability of these measurements for a clinically available MR-SIM system.

2) To evaluate the distortion phantom design needs of the MR-SIM community based on available technology and develop a modular large FOV phantom that can be made using easily obtainable materials and optimized for many MR systems. In-house distortion characterization methods from Aim 1 are used to develop platform independent software optimized for several MR systems and integrated into a widely available medical imaging application, 3DSlicer.[61]
3) To determine equivalence between synCT and CT for IGRT by benchmarking results in a novel MR-CT compatible brain phantom and performing an analysis in a cohort of brain cancer patients across multiple IGRT platforms.

Overall, by focusing on some of the remaining unknown inaccuracies in MR-only RTP and laying further groundwork for integration of methods into the MR-SIM workflow, the completion of this work will further support the widespread clinical implementation of MR-only RTP.

CHAPTER 2 "GRADIENT NONLINEARITY DISTORTION OF A 1T OPEN BORE MR-SIMULATOR"

Introduction

Magnetic Resonance Imaging-Theory and Background

While CT derives its signal from the electron density of the object being imaged, MRI relies on the net magnetization of hydrogen atoms within the object. Normally, the net magnetization is zero, as magnetic field vectors for each hydrogen atom are randomly distributed. However, MRI creates a net magnetization by applying a large external field (B0), effectively aligning the nuclear spins along the field and creating a two-state system: spins aligned with the B_0 field (parallel), and spins aligned against the B0 field (anti-parallel). The parallel spin state is a lower energy level than the anti-parallel state, and as a result there are slightly more spins aligned with the field than against it, creating a net magnetization in the direction of B_0 known as longitudinal magnetization.

While in the external B_0 field, all spins will precess about the B_0 axis at a resonance frequency known as the Larmor frequency, which is directly proportional to the magnitude of this external field as shown in equation 1.1.

$$\omega_0 = \gamma B_0 \tag{1.1}$$

This precession would cause a component of net magnetization, known as transverse magnetization, which is perpendicular to the B_0 axis. However, at equilibrium the precessions of these spins are out of phase, resulting in a net transverse magnetization of zero. If a 90 degree radiofrequency (RF) pulse is applied, these spins become coherent while some of them are excited from parallel to anti-parallel, temporarily

creating a non-zero transverse magnetization and decreasing the longitudinal magnetization, effectively 'tipping' the net magnetization vector by 90 degrees.

Once the RF pulse is turned off, the spins immediately begin transitioning back to the ground state in a process called 'relaxation'. Longitudinal, or 'spin-lattice' relaxation, refers to the dissipation of energy between spins and the surrounding lattice, resulting in the return of some excited spins from anti-parallel back to parallel, and a gradually increasing longitudinal magnetization. This relaxation is characterized by time constant T1, which is the time required to return to 63% ($1-e^{-1}$) of the original longitudinal signal. Transverse or 'spin-spin' relaxation, characterized by T2, refers to the theoretical gradual decay of the transverse signal as spins interact with each other and fall out of coherence. However, in application, any inhomogeneities in the external field cause the transverse signal to decay much faster than predicted, and is therefore characterized by the much smaller T2*. Using coils oriented orthogonally to the B0 axis, the signal resulting from this changing magnetic field can be recorded, and the three time constants, which are tissue dependent, together make up the basis of image contrast in MRI. However, to reconstruct an image from this signal, it must also contain spatial information.

The localization of MR signal relies on the successive application of magnetic field gradients. For a 2D acquisition, a magnetic field gradient called the slice selection gradient is first applied perpendicular to the desired slice plane. In accordance with the Larmor frequency equation presented above, this will cause the precessional frequencies in the object to vary with position. An RF wave can then be applied with the same frequency as the desired slice plane, causing a shift in the magnetization and the

selective excitation of only atoms within this plane, such that other planes will not emit a signal.

Within the excited plane, the signal can be further localized by spatially encoding the signal with two additional gradients. The phase encoding gradient, in the simplest case, is a magnetic field gradient applied for a short time before the acquisition of each row of pixels. At the time of acquisition, this results in protons which precess at the same frequency, but at slightly different phases of precession along the axis of the gradient. Lastly, a frequency encoding gradient is applied perpendicular to the previous two gradients during signal acquisition, allowing for spatially varying frequency of signal in the final axis. Once acquisition is complete, each voxel of the final dataset will be associated with a unique combination of frequency and phase, allowing for an image to be reconstructed by taking the inverse Fourier transform of the data.

A 3D acquisition is accomplished similarly with both frequency and phase encoding, with an important difference in the slice selection process. Rather than selectively exciting a single slice, the image is instead acquired with an additional phase encoding step in the slice selection direction. The data is therefore acquired as a volume, and reconstructed with the inverse 3D Fourier transform.

Geometric Distortion

The geometric fidelity of MRI relies on accurate spatial encoding of spins throughout the imaging region, which is done under the assumption that the B_0 field is homogeneous and the spatial encoding gradients are linear. While these assumptions are generally true within a small FOV, they tend to diverge from the real solution as you move farther from isocenter.[28, 62, 63] If the resulting magnetic field differences are large

enough, errors can propagate through the spatial encoding process, and present as geometric distortions in the final image. These distortions can be both system dependent and/or patient dependent, and where they originate helps determine the best approach for handling them.

System-dependent distortions arise from inhomogeneity of the B_0 field, and from spatial encoding gradient non-linearity (GNL). While GNL induced distortions exist in all three gradient axes, typical acquisition sequences fill a single line of k-space for each excitation pulse, thus only encoding B_0 field distortions in the frequency encoding axes. For a typical 2D acquisition sequence, this would result in B_0 field distortions in the read encoding and slice selection direction. However, as 3D acquisition sequences utilize further phase encoding in the slice select direction, these sequences can isolate B_0 field distortions to only the read encode axis.[50]

Patient-dependent distortion further contributes to B_0 field distortion. When a patient is placed in the bore, the magnetic field is perturbed by additional induced fields, creating further inhomogeneity. While additional shimming can be done to correct this global effect, materials with different susceptibilities result in different induced fields while in the magnet, and these local field variations can result in non-negligible frequency shifts near the boundaries of objects with large susceptibility differences (air/tissue interfaces) in the frequency encoding direction. Also, due to electron shielding, the precessional frequency of fat is shifted which can result in further positional inaccuracies near water/fat boundaries in an effect called chemical shift.

The patient-dependent distortions can be minimized through thoughtful sequence selection (larger gradients to reduce the amount of pixel shift resulting from B_0 field

inhomogeneity). While some situations may necessitate the implementation of patient-specific post-processing correction maps, patient-dependent distortions have been shown to depend on field strength, and can be considered clinically negligible for low field systems,[64, 65] such as our 1.0T MR simulator. System-dependent distortions can be minimized by imaging as much of the FOV near isocenter as possible. Paulson et al. facilitated this by physically stepping the patient through the magnet to acquire the total image in parts.[30] GNL distortions can be further corrected using a post-processing technique to warp the image, or by improving the gradient field model with higher order spherical harmonics. Since GNL distortion is one of the dominant sources of image distortion[46, 49] and is independent of acquisition sequence,[66] this chapter focuses on the technical characterization of GNL distortion for large FOVs, develops and evaluates a correction scheme, and then quantifies the temporal stability of the measurements for a clinically available MR-SIM system.

Materials and Methods

Large FOV Distortion Phantoms

For temporal GNL measurements, a 36x43x2 cm^3 2D distortion phantom (Philips Medical Systems, Cleveland, OH) consisting of 255 capsule-shaped landmarks with ~4mm radius and 25mm centroid-to-centroid spacing was used. The phantom can be oriented in all three cardinal axes (axial, sagittal, and coronal), allowing for 2D images of the control point array to be acquired quickly for each image orientation (see figure 4). For full 3D distortion characterization, a 465x350x168 mm^3 phantom with over 4600 control points and 1.6cm centroid-to-centroid spacing was used (figure 2).

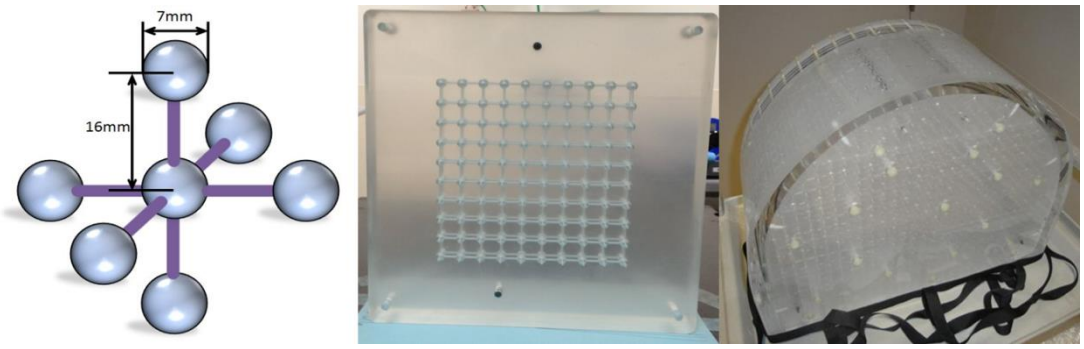

Figure 2: (Left) Control point design, (Middle) one finished plate, and (Right) the completed build for the 3D distortion phantom.

Image Acquisition

MR images were acquired with our 1.0 T MR simulator using the integrated quadrature coil. Our MR simulator is an open bore design with a vertical magnetic field, and 45 cm anterior-posterior (A-P) clearance of the physical aperture. To measure distortions resulting from GNL, the phantom was scanned with a 3D T1-weighted gradient echo (GE) sequence: TE/TR/flip angle of 5.54 ms/30 ms/28°, FOV 450x450x26 mm^3, bandwidth 191 Hz/pixel, acquisition voxel dimensions 1x1x2 mm^3, number of signal averages = 1, and acquisition duration of 5.6 minutes. This effectively isolates distortion resulting from susceptibility and B_0 inhomogeneity to a single axis in the read encoding gradient direction. So, by obtaining two scans of in each of the three phantom orientations (the first scan with a positive read gradient polarity 4.48 mT/m and the second with a negative read gradient polarity -4.48 mT/m), the polarity of B_0 distortions will be reversed between the two scans. This allows for the reverse gradient technique to be utilized, which takes the average position of each control point, thereby removing the effects of all distortion except for that due to GNL.[44, 46, 65] Our scanner is already equipped with vendor-supplied corrections that utilize a spherical harmonic model of the gradient fields to correct for GNL related distortions. Therefore, the goal of this study

was to acquire all images with vendor-supplied 3D corrections enabled, as is consistent with our clinical practice, and perform all analyses on the residual distortion.

For the 3D phantom analysis, in order to sample the distortion over the full superior-inferior (S-I) scanning FOV, a batch file script was devised that communicates with the MR scanning software to translate the 3D phantom in the axial orientation and scan at three different overlapping positions to yield a total extent of 465x340x400mm^3 (>13,800 landmarks). Two scans with reverse read gradient polarities were taken at each of the 3 locations within the bore so that the reverse gradient technique could be applied and characterize only the GNL distortion throughout the entire imaging volume.

As a feasibility study, the 2D phantom was also used to characterize the full 3D FOV using the batch script method to step the phantom throughout the bore (we will refer to this method as 2.5D to differentiate from the true 3D phantom). The phantom was setup in the axial plane, and stepped through 15 different locations 2.5cm apart, for a characterized FOV of 35x40x35cm^3. To validate the accuracy of this method, the correction map generated from the 2.5D method was used to correct an image of the 3D phantom, and residual distortion in this image was characterized.

It has been shown that eddy currents generated by rapidly pulsed gradients may potentially influence image distortion.[50] To verify that eddy currents do not adversely impact our distortion characterization, the phantom was scanned as above at 4 different Echo Time (TE) settings (5.5, 13.8, 20.7, and 34.5 ms with TR=50.9 ms) in all three cardinal axes. TEs spanned a range similar to what has been reported in the literature, but modified *ad hoc* to yield acceptable image quality and resolve scanner conflicts. Using 5.5ms as the baseline value, the mean shift in distortion measurements over all

landmarks for each phantom orientation was calculated and plotted as a function of TE to identify possible trends.

Image Analysis

To establish the position of each phantom control point (defined as the centroid), an automated program was developed in-house using MATLAB® (Mathworks, Natick, MA). First, images were generated by taking the maximum intensity projections through all 13 slices of each 2D phantom scan, which is consistent with our clinical protocol.[28] Control point detection was then conducted on each image with a combination of masking and thresholding, while a connectivity algorithm and some basic morphology techniques were employed to further separate control points from the increased noise at the periphery of the field. The x and y positions (horizontal and vertical axes respectively) were determined by finding the centroid of each control point and were compared to a binary template generated from the factory schematic of the phantom. Similar analysis was performed for the 3D phantom for all three axes. The total distortion of each control point was taken as the difference of the measured centroid positions from the known position in the template. Once the distortions at each control point were determined, a full distortion map was interpolated by using singular value decomposition (SVD) to fit the data to a polynomial. Both Hong *et al*.[67] and Wang *et al.*[68] studied the deviation of various polynomial models (for orders 3-7 between both studies), and found sixth-degree polynomials had the smallest mean and maximum deviations from measured values. After a similar small study of various models was performed(see Appendix A), the sixth-degree polynomial was chosen for the final model. This polynomial can be written as shown in equation 2.2:

$$r' = t + Ar + Br^2 + Cr^3 + Dr^4 + Er^5 + Fr^6 \quad (2.2)$$

Where A is the matrix of coefficients defining first-degree transformation components such as translation, rotation, and shear, B is the matrix of second-degree coefficients, C defines third-degree, D defines fourth-degree, E defines fifth-degree, and F defines sixth-degree coefficients. Once the coefficients are determined, full distortion maps are generated for the original image grid, and the maps were plotted and compared for each axis (week 1 shown in figure 4), and over the entire sampled FOV using the 3D phantom.

Distortion Correction

To correct for the distortion, the derived distortion map was used as a template to warp the distorted images and create a corrected image. However, since there is not necessarily a one-to-one correspondence between pixels in the distorted image and pixels in the corrected image, our algorithm utilizes a reverse warping methodology by stepping through each pixel of the corrected image and determining the pixel's intensity from the distorted pixels that map to it. This ensures that no pixels in the corrected image are missed, and thus avoids "holes" in the corrected image. Also, since image distortion may cause compression and expansion of image volumes resulting in intensity changes that may not be fully resolved by pixel mapping, the corrected image was also multiplied by a Jacobian scaling factor as determined by equation 2.1.

$$J(x,y,z) = \begin{vmatrix} 1+\partial[\Delta x]/\partial x & \partial[\Delta x]/\partial y & \partial[\Delta x]/\partial z \\ \partial[\Delta y]/\partial x & 1+\partial[\Delta y]/\partial y & \partial[\Delta y]/\partial z \\ 1+\partial[\Delta z]/\partial x & 1+\partial[\Delta z]/\partial x & 1+\partial[\Delta z]/\partial z \end{vmatrix} \quad (2.1)$$

Temporal Stability of Distortion Corrections

Temporal stability of large FOV distortion corrections and recommended measurement frequency is not well known. Mah et al. measured distortion at 4 locations and showed temporal variations of less than 3 pixels over 18 months, although this was not characterized for large FOVs.[69] To characterize the stability of GNL distortion measurements, weekly scans of the 2D distortion phantom in all three axes were acquired over the course of 18 months (23 time points) using the reverse gradient technique.

Results

2D Distortion Characterization at Isocenter

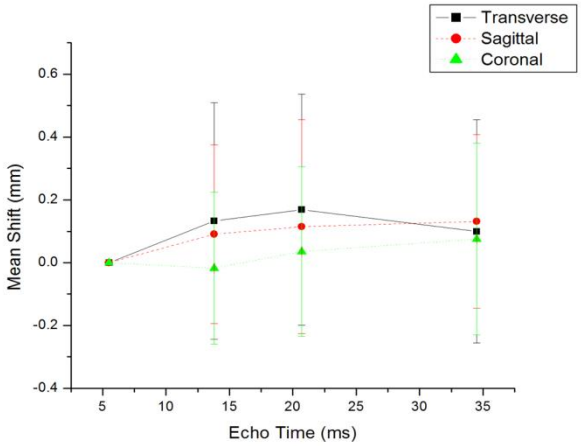

Figure 3: Mean shift in distortion measurements over all landmarks as a function of acquisition TE for all three phantom orientations.

As demonstrated by Figure 3, eddy currents were found to be appropriately compensated for with image distortion varying <0.2mm (less than half the pixel width) over all TE settings. Figure 4 shows the maps of residual distortion resulting from GNL in the three cardinal planes at magnet isocenter, and Table 1 shows the corresponding distortion statistics across the entire 36x43cm phantom. While less than the 1mm pixel width near isocenter, these distortions become greater than 1mm as close as 9.5cm from isocenter in the transverse plane, 12.5cm in the sagittal plane, and 11.7cm in the

coronal plane. The largest distortion magnitudes occurred near the periphery of the usable FOV (~4mm distortion at 20cm from isocenter), where the usable FOV is defined by the furthest extent at which control points can be identified.

Plane	Mean (mm)	StDev (mm)	P5 (mm)	P95 (mm)	Distortion > 1mm (Total % Pixels)	Distortion > 2mm (Total % Pixels)
Transverse (x)	0.07	1.10	-1.83	1.92	35	7
Transverse (y)	0.10	1.10	-1.5	2.15		
Sagittal (x)	0.03	0.64	-0.93	1.15	14	3
Sagittal (y)	-0.09	0.70	-1.23	1.11		
Coronal (x)	0.40	1.16	-1.32	2.50	40	14
Coronal (y)	0.04	0.40	-0.52	0.77		

Table 1: Week 1 gradient nonlinearity distortion statistics for three cardinal planes through isocenter where x and y refer to the horizontal and vertical axes of the respective plane. P5 and P95 describe the 5th and 95th percentiles of the distortion distribution, respectively.

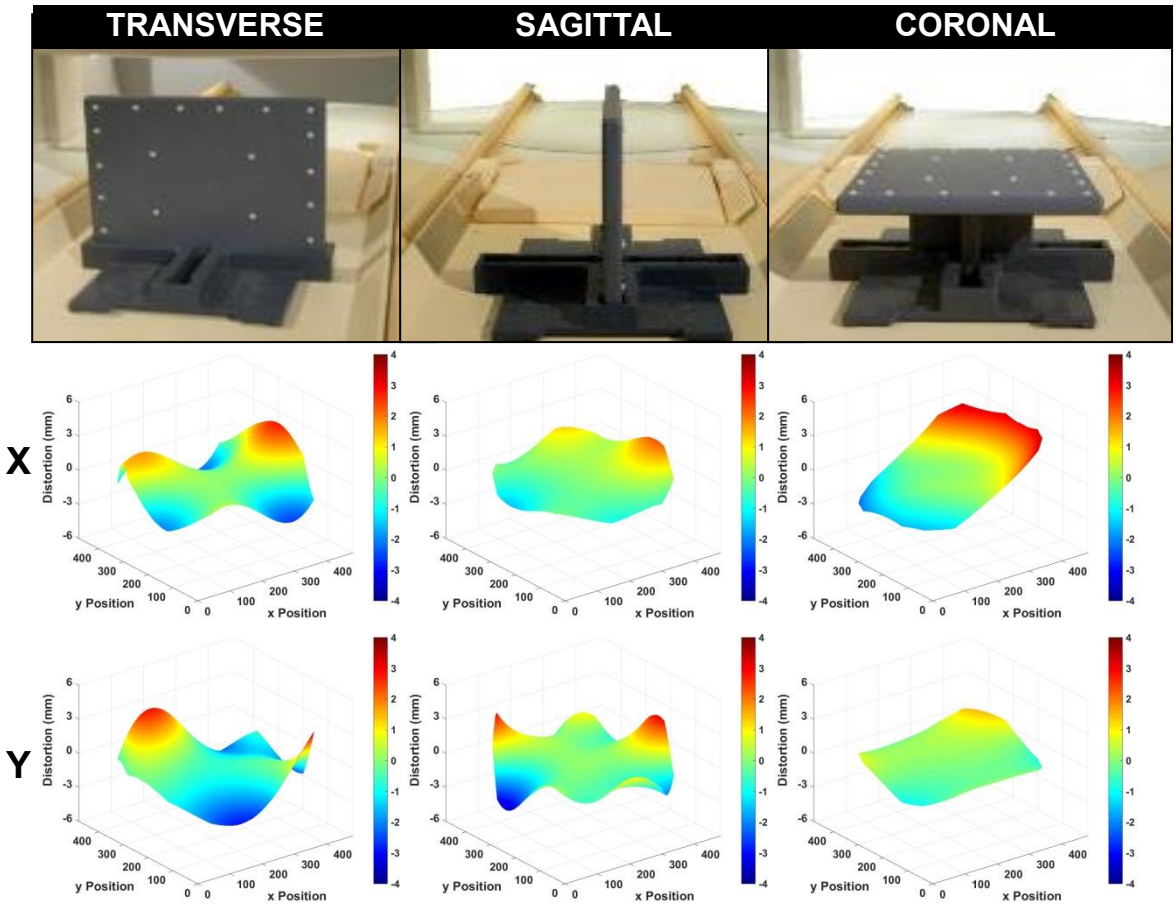

Figure 4: (Top Row) Setup of 2D distortion phantom (Middle Row) corresponding x-axis distortion map (mm) vs image pixel location (Bottom Row) corresponding y-axis distortion map (mm) vs image pixel location

For the temporal analysis over 18 months (Figure 5), the coronal plane had the widest interquartile range, with 50% of the usable FOV having distortions between -0.5 and 1.25 mm, while the sagittal plane had the smallest, with 50% of the usable field of view having distortion between -0.25 and 0.25 mm. The transverse plane consistently has the largest distortions with maximum distortions of 4mm, and a P95 of 2mm. However, for any given daily distortion measurement over the 18 months, difference maps show 95% of voxels varied <0.6 mm from the baseline measurement (week 1) for all planes.

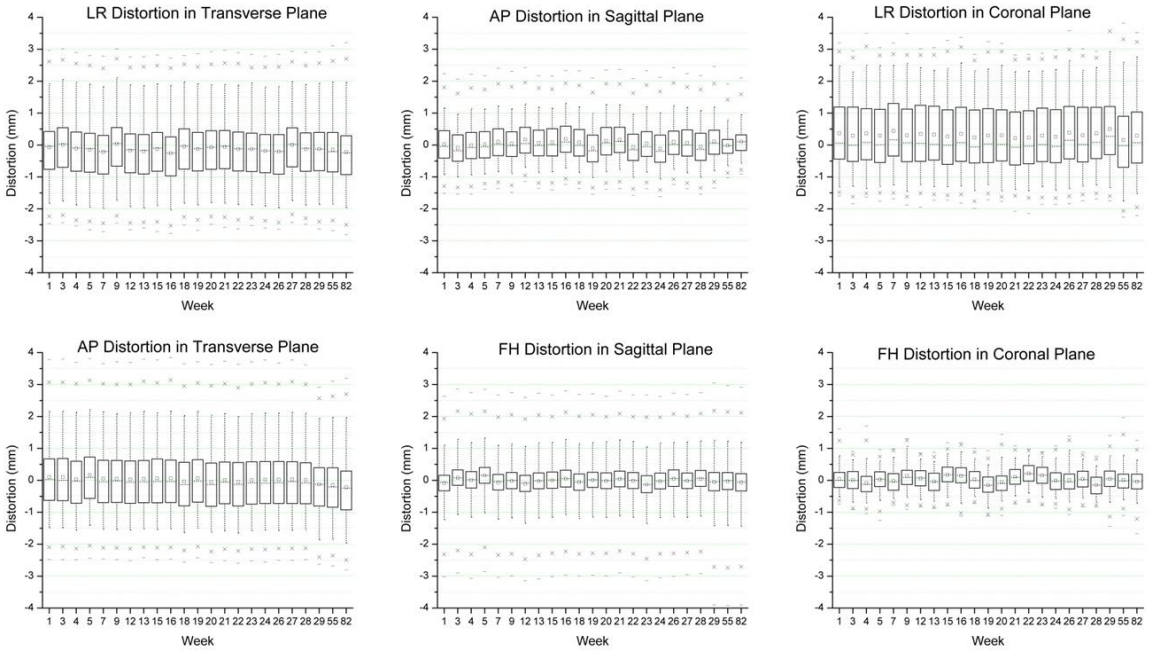

Figure 5: Distribution of gradient non-linearity distortion measurements over 82 weeks. Boxplots, dotted line and circle indicate interquartile range, mean, and median respectively. Whiskers indicate 5th and 95th percentile, x's mark 1st and 99th percentile, and dashes mark the minimum and maximum distortions.

2.5D Distortion Characterization

Figure 6 shows the residual 3D distortion after corrections from the 2.5D data were applied. The correction used was least affective for in the SI direction with >1mm distortions still present at radii larger than about 10cm from isocenter. While for L-R and A-P directions, the 2.5D distortion corrections maintained less than 1mm distortion for most of the FOV. However, the residual distortions in all three directions were non-negligible near the periphery of the field.

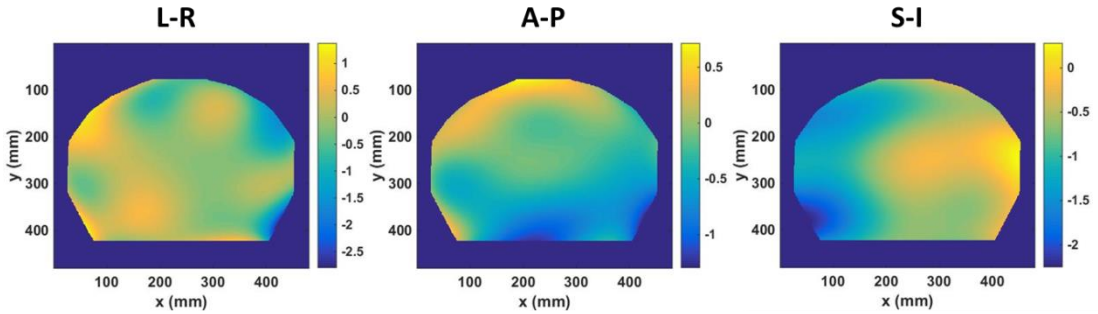

Figure 6: All three components of distortion after correction with 2.5D correction map at a single plane near isocenter.

3D Distortion Characterization

As expected, distortion from GNL is much more pronounced in the peripheral voxels. Over the entire sampled volume, 65% of all voxels had non-negligible distortions (>1mm), 26% of voxels distorted > 2 mm, 9% > 3mm, and 3% > 4 mm, with the largest distortion observed of ~7.4 mm at 23 cm radial distance from magnet isocenter. Figure 7 illustrates the 3D distortion results at one particular slice of the phantom volume (-15cm from isocenter) before and after post-processing corrections were applied, while figure 8 shows a 3D rendering of the same results. In the post-correction dataset, nearly all measured distortions were reduced to less than 1 pixel width, with the exception of distant field corners up to a radial distance of 25 cm from magnet isocenter.

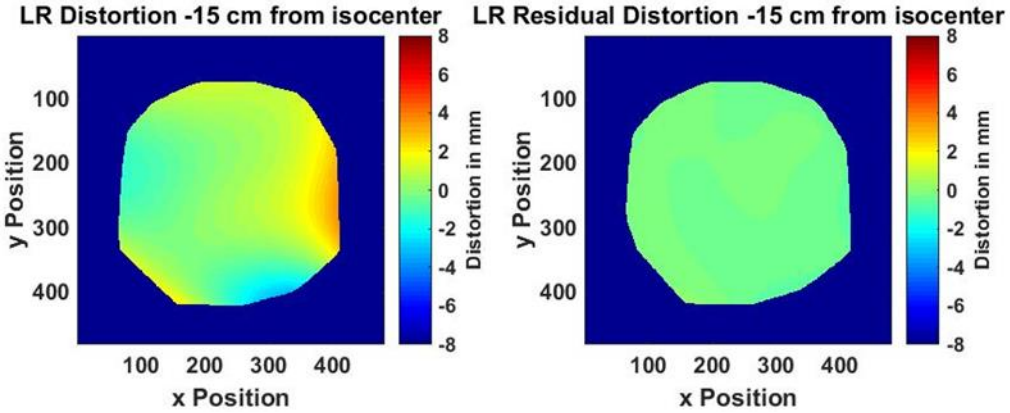

Figure 7: Left-right (LR) distortion maps for the 3D phantom in the transverse plane. (Left) Quantified gradient non-linearity distortion for the 3D phantom at 15 cm inferior of isocenter. (Right) Residual distortion after post-processing corrections were applied.

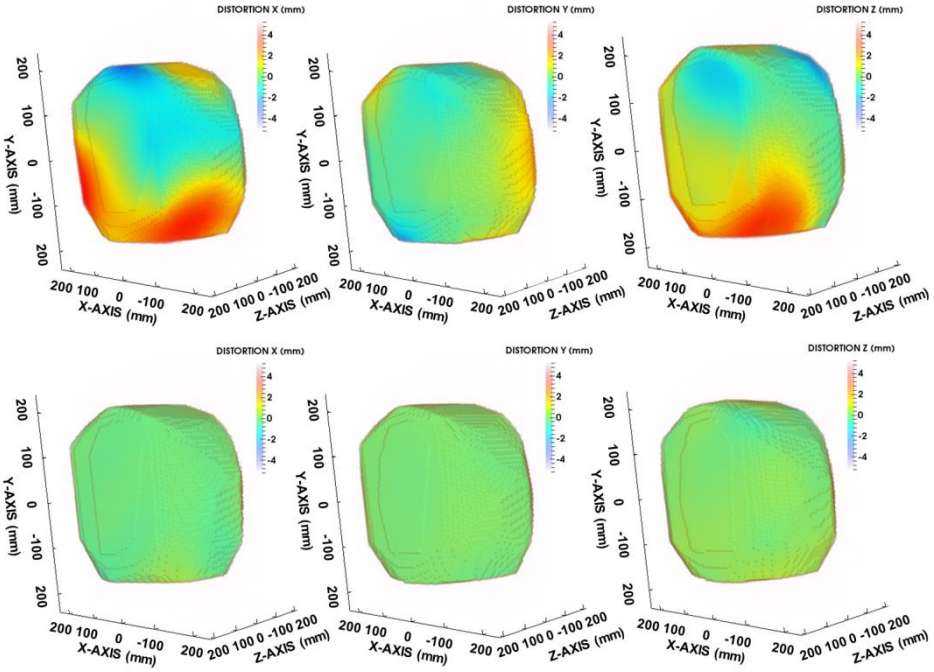

Figure 8: (Top Row) A 3D rendering of the each component of the gradient non-linearity distortion for the 3D phantom. (Bottom Row) A 3D rendering of the esidual distortion after post-processing corrections were applied.

Figure 9 shows the 3D stepped distortion map data plotted as a function of radial distance from magnet isocenter with the radii of typical anatomical structures also shown.[63, 70-73]. Initial vendor-supplied 3D distortion corrections maintained <1mm distortion up to ~9.5 cm from isocenter although GNL became non-negligible as distance from isocenter increased.

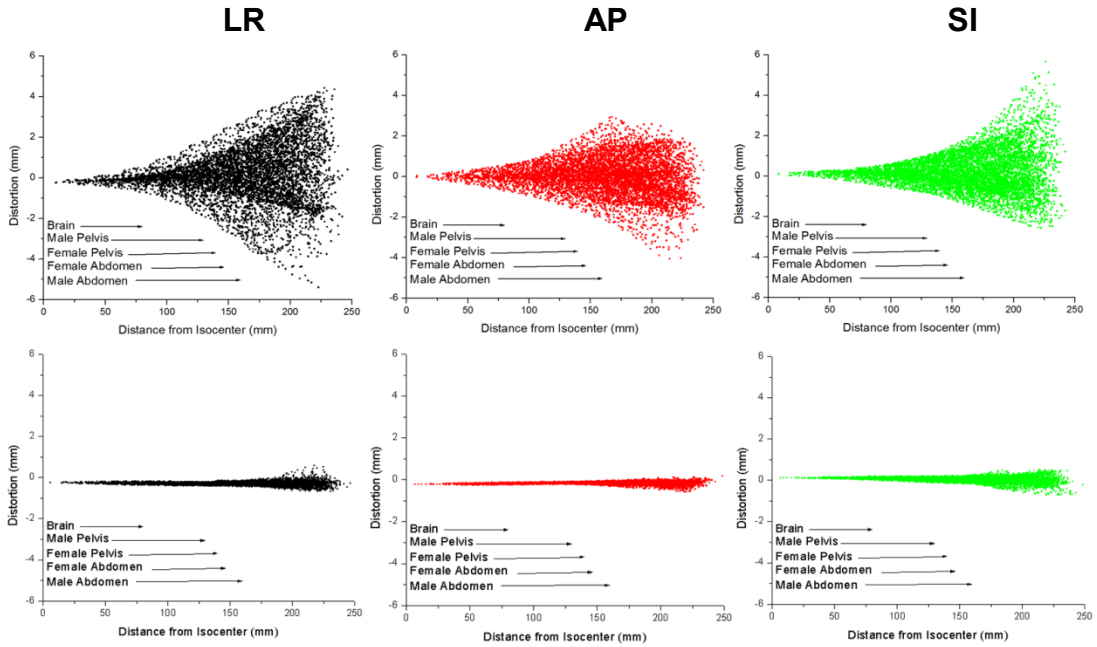

Figure 9: (Top Row) Distortion measurements (mm) as a function of distance from magnet isocenter (mm) for one scan. (Bottom Row) Residual distortion after post-processing corrections (mm) as a function of distance (mm). Arrows show the average radius of relevant anatomy of interest taken from the literature.[71-73]

Discussion and Conclusion

The eddy current analysis was in good agreement with Baldwin et al. (<0.3mm for a 3T cylindrical bore magnet).[46] In 2000, Tanner et al. measured distortions of up to 1.3mm with varying TE for their 1.5T cylindrical bore magnet[50]; however, early generation magnets like this one contained unshielded gradients, while modern hardware (shielded gradients) more readily compensates for eddy current effects.

The planar distortion at isocenter shown in figure 4 is similar in magnitude to those measured without vendor corrections enables on a 3T cylindrical bore magnet by Baldwin et al.[46] For our vertical magnet geometry, the maximum magnetic field gradient occurs in the right to left direction, which may contribute to the larger GNL distortion in this axis. It is also important to note that our measurements were non-negligible when 3D vendor distortion corrections were enabled, indicating that additional corrections are necessary for our magnet configuration. However, the temporal data suggests that for

routine QA, a higher frequency of GNL measurement is not necessary and these results support recent recommendations of annual measurement.[30]

The feasibility study using 2.5D corrections showed that while corrections for L-R and A-P directions were effective up to about 18cm from isocenter, the residual S-I distortion was not improved. This is likely a result of less rigidity and accuracy of our experimental setup in the S-I direction. However, the effectiveness of the 3D stepped distortion correction shown in figures 7-9 suggests that with appropriate post-processing corrections, GNL distortions can be reduced to negligible levels despite substantial initial GNL distortion for large FOVs. Similar results were reported by Doran *et al*.[47] and Baldwin *et al*[46], with a possible cause of the remaining distortion being divergence of the polynomial fit at the boundaries. When plotted as a function of radial distance from isocenter, this data suggests that to support MR-only RTP, additional corrections are necessary for anatomy > 10 cm from isocenter for this magnet configuration. However, in another study by Wang et al., it was suggested that shorter gradient coils could result in significantly higher GNL distortion[49], which suggests that the GNL distortion measured for vertical magnet designs could be significantly worse than for the more commonly used cylindrical bore configuration.

As discussed earlier, another potential solution to address GNL includes using a "step and shoot" technique where multiple couch longitudinal positions are used to segment large FOVs to facilitate imaging more of the anatomy of interest near isocenter[30]. Our open geometry allows for lateral table translation, thus lateral lesions such as breast cancer or sarcomas may be positioned at isocenter to further reduce the impact of GNL.

One limitation of this study is that it focused on GNL and did not address other sources of distortion such as those arising from field inhomogeneity, chemical shift, and magnetic susceptibility differences. Nevertheless, using higher readout bandwidths[30, 65, 74] and thoughtful sequence selection[75] have been shown to minimize these effects. A double echo gradient echo phase mapping method[65, 76] can be used to measure and calculate sequence-dependent distortion maps which can then be used for corrections. Future work will include characterization of patient-dependent distortions for our magnet, including susceptibility, for relevant regions of interest. In addition, while we chose to use a polynomial model in this study, there is potential for better modeling of the gradient fields by utilizing spherical harmonics. This could be done by performing a deconvolution NMR plot of the gradients fields in isolation. The mapping from distorted to undistorted space could then be done iteratively, and then resampled to a regular grid. Studies have investigated the potential of this type of method, and it is possible that further refinement of the spherical harmonic coefficients utilized in vendor corrections could improve the distortion on our magnet.[45]

Another limitation of this study is the lack of validation of our Jacobian intensity scaling approach. Also, given the nature of this filter, it is important to note that using this correction could result in image quality degradation. While no image quality analysis is included in this study, figure 10 has been included as a case example and shows one slice of both the corrected and uncorrected patient images. It is apparent by looking at anatomical changes relative to the uncorrected boney contour that geometric differences do exist between the two images, however image quality differences are not immediately obvious. Possible blurring may occur near the periphery of the patient

where larger corrections were necessary; however an image quality study would be necessary to fully characterize these differences.

Figure 10: (Left) Coronal pelvic image of a patient from our 1T open bore MR scanner with only vendor corrections applied, (Center) with additional post processing corrections, and (Right) a subtraction image of the corrected and uncorrected images. Boney contour was drawn on uncorrected image, and propagated to the corrected image to highlight geometric changes.

Inherent distortions due to GNL were non-negligible for large FOVs with 3D vendor corrections enabled, thus necessitating a correction scheme to support MRI only treatment planning for anatomies >10 cm from isocenter. However, with post-processing corrections, GNL was reduced to <1 mm for large FOVs. GNL measurements were stable over 18 months of clinical operation, thus supporting the application of correction maps in MR-only RTP. Further work could be done to improve the initial vendor correction with higher order spherical harmonic coefficients, while investigation of a dynamic solution for patient-specific distortions is warranted.

CHAPTER 3 "OPTIMIZATION OF A NOVEL LARGE FOV DISTORTION PHANTOM FOR MR-ONLY TREATMENT PLANNING"

Introduction

The system-specific distortions discussed in the previous chapter have been shown to increase with increased distance from isocenter, making accurate measurement and correction over large fields of view (FOVs) important for radiation treatment planning involving anatomy away from isocenter.[62] Many studies have evaluated large FOV distortions using in-house phantom designs. Early designs include Tanner *et al,* who utilized orthogonal arrays of water-filled polymethyl methacrylate (PMMA) tubes to characterize a volume of 40x25x40cm^3(in the left-right (L-R), anterior-posterior (A-P), and superior-inferior (S-I) axes respectively).[50] While the PMMA tubes have small susceptibility differences from water, they also expanded/contracted substantially with temperature changes, and necessitated the use of free-sliding seals at tube support positions. Breeuwer *et al* first used a 3D array of point-like landmarks[51] while Wang *et al* used a 3-dimensional (3D) grid spanning a 31x31x31 cm^3 volume.[77] Both of these phantoms required a fluid filling to serve as contrast from the markers. More recently, Huang *et al* devised a hybrid design comprised of regularly spaced spherical cavities connected by channels in a grid-like pattern.[52] This design also utilized liquid contrast filling, but unlike the others, directed the contrast into the hollow landmarks themselves, creating the potential for air bubbles. Also, while large in the axial plane (46.5x35cm^2), they did not provide full S-I FOV characterization, spanning a distance of only 16.8cm in that dimension. Walker *et al* developed a full FOV distortion phantom, utilizing an array of vitamin E capsules over a 50x51.3x37.5cm^3 (L-R, S-I, AP) volume. While much work exists on distortion phantom development, very few of the

phantoms provide sufficient large FOV coverage, and those that do have been customized to meet the geometry requirements for a single MR system. While phantoms have been designed, the availability of comprehensive distortion analysis software is also currently limited. The goal of this work was to evaluate the phantom design needs of the MR-SIM community based on available technology and develop a modular large FOV phantom that can be optimized for many MR systems and made using easily obtainable materials. Lastly, in-house distortion characterization software was optimized for several MR platforms and integrated into a widely available medical imaging application platform, 3DSlicer.[61] Importantly, the modular phantom design and availability of standardized analysis can be used to facilitate collaboration and perform benchmarking for multi-institutional trials of MR-only treatment planning.

Materials and Methods

Phantom Materials

The phantom design utilized in this work was adapted from a previously described study [78] that used a stack of low density polyurethane foam plates (6 lbs/ft^3, 2.5cm thick) with 6 mm paintball inserts (polyethylene base) as signal generating control points (available at: www.MCSUS.com, UPC: 844596050069). While the original phantom design was lightweight, the low-density foam was found to be pliable and easily damaged, making long-term stability of the phantom's geometric integrity a potential concern. To build a more robust phantom with a material that could withstand transport to multiple Radiation Oncology centers for benchmarking, twelve urethane foam based materials of various density and strength characteristics (4-40lbs/ft^3 and 8-72 Shore D hardness, where Shore D is a hardness scale commonly used for plastics

and elastomers [79]) were identified. Test slabs were custom machined by Non-Magnetic Specialties for each candidate material (25 ± 0.25 mm center-to-center spacing, ~6.5 mm deep using a ~6.4 mm ball nosed endmill) and 6 mm paintballs were inserted into the foam. MR and CT images were acquired to assess the paintball signal strength relative to each background material. Because CT will serve as the "ground truth" image for distortion calculations, intensity-based automatic segmentation of the paintballs from the background material was an important consideration. Final material selection was performed based on a balance of strength, weight, machinability, and cost.

Bore/Phantom Model

Bore sizes and minimum aperture widths (smallest diameter of clearance within the bore once the couch is positioned inside) were tabulated for fourteen MR systems and one MR-IGRT system across five vendors (table 2). An in-house MATLAB® (Mathworks, Natick, MA) script was used to generate shape models of each bore to simulate the position of the phantom within each configuration and assess the clearance of the phantom (assuming a flat table top), with the overall endpoint of determining the optimal phantom configuration required for each MRI bore. Plates varied in width such that the widest plates were positioned near the widest portion of the bore (magnet isocenter) and tapered in size towards the bore periphery. A variable phantom design was input into the script, allowing for optimization of the plate width and total number of plates required for each configuration, such that there was adequate clearance while still characterizing the full imaging volume. In order to simplify the model, the script assumes a circular cross-sectioned bore for all MR systems other than the Panorama

high-field open (HFO), and a flat couch-top. Nonetheless, it was useful for visualization and planning of the final phantom construction.

MR System Vendor	Model	Bore Size (cm)	Min. Aperture (cm)	FOV (cm^3)
GE	Signa (1.5T)	60	46.5	48x48x48
	Optima MR450w	70	52	50x50x50
	Discovery MR750w			
Philips	Intera	60	42	53x53x53
	Panorama	open	45	45x45x45
	Achieva	60	42	53x53x53
	Ingenia	70	53	55x55x50
Siemens	Symphony	60	45.2	50x50x50
	Avanto		45.5	
	Aera	70	55	
	Skyra			
	Verio			
Toshiba	Vantage	60	48.3	50x50x50
	Titan	69	52.9	55x55x50
ViewRay	MRIdian	70	55	50x50x50

Table 2: Bore sizes, FOV, and minimum aperture widths resulting from couch position tabulated for fourteen MR and one MR-IGRT systems across five vendors.

Software Design

In-house image processing software was developed in C++ to automatically generate geometric distortion maps from phantom DICOM MRI data using similar techniques described in detail in our previous work (section II.D)[62] assuming the reverse gradient methodology is used. First, thresholding and masking techniques were employed for detection of paintball control points in both the CT and MR image. The data was then filtered to remove extraneous or unusable information using a connectivity algorithm with basic morphology techniques, and control point positions

were calculated by finding the centroids of the remaining markers. The central control point is then identified on both the MR and CT image, and combined with DICOM header information to perform a coordinate transformation of the CT control point positions to the MR coordinate space. Total distortion at each control point was then calculated by measuring the difference between MR control point positions with those generated from a reference CT image. Full distortion maps could then be generated across the entire FOV by interpolation using singular value decomposition to fit the data to a sixth-degree polynomial as previously implemented.[62, 68]

To make our work widely available to the community, we integrated our distortion characterization software into the 3D Slicer[61] application platform. 3D Slicer is an extensive medical image processing toolset, widely available open-source code, and modular design that is designed as a plugin framework. This then allowed for our distortion software to be written as a loadable C++ module that can utilize any of the robust C++ libraries already integrated into the 3D Slicer core. Specifically, our module uses existing DICOM import plugins, as well as existing VTK[80] visualization mechanisms, Qt[81] for user-interface construction, and both ITK[82] and VTK for image processing. C++ also offers the advantage of faster run-times as compared to MATLAB and other computing software.

Software Validation

To evaluate the software performance, GNL was evaluated for our 1.0T HFO MR-SIM and compared against our previously published results using MatLab and a different large FOV distortion phantom. Distortion maps were compared directly via difference maps within the FOV covered by both phantoms. Global distortion statistics

(including the percent of voxels distorted over 1, 2, 3, 4, and 5 mm and maximum distortions) were also compared between approaches, and comparisons in polynomial data fits were evaluated based on the mean absolute error. Finally, distortion maps were plotted as a function of radial distance from isocenter to compare the overall distribution of new distortions maps with those that we have previously validated.

Multi-magnet Characterization

CT reference images were acquired of the phantom in each configuration using a large-bore multislice CT scanner (Brilliance^{TM} CT Big Bore v3.6; Philips Health Care, Cleveland, OH) at 120kVp, 344mAs, and voxel dimensions 1x1x2mm^3. MR images were acquired on three MR systems, including a 1.0 T Panorama High-Field Open, 1.5 T wide bore Ingenia, and a 3.0 T Ingenia (Philips Medical Systems, Cleveland, OH). All images were acquired using integrated quadrature coils with a 3D T1-weighted GE sequence (see table 3 for acquisition parameters).

	1T Panorama	1.5T Ingenia	3.0T Ingenia
TE(ms)	5.5	4.4	2.98
TR(ms)	30	30	31.74
Flip Angle(°)	28	28	28
Acquisition Matrix	432/430	432/433	296/297
Bandwidth (Hz/pixel)	190	190	433
Reconstructed Voxel Size (mm^3)	0.96x0.96x2	0.77x0.77x2	0.61x0.61x2
Signal Averages	1	1	1

Table 3: MRI acquisition parameters for each of the three MR systems tested in the multi-magnet characterization study.

Two scans were obtained for each MRI acquisition with the second acquisition identical except for the reversal of the read gradient polarity. In this manner, the GNL induced distortion could be isolated from total distortion using the reverse gradient methodology,[44, 46, 62, 65] and allowed for generation of patient independent distortion correction maps. Standard 3D GE imaging protocols utilize phase encoding for two axes with only 1 frequency encoded axis, which isolates object dependent and B_0 related distortions to this axis, as they are only present in frequency encoding directions. Distortions resulting from GNL are present in all directions, and are independent of acquisition sequence. Also, when the polarity of the read gradient is reversed, the polarity of any B_0 distortions will also be reversed, while GNL distortion remains constant, and thus, the GNL distortion can be isolated by taking the average distortion between the two scans. All scans were acquired with vendor supplied 3D geometry corrections enabled. MR and CT scans for 3 phantom configurations were then uploaded into 3DSlicer for further GNL and distortion analysis. Also, as each MR system produced images of different contrast, resolution, and signal to noise, the parameters utilized for thresholding and object identification were changed for each magnet to yield optimal results.

Results

Final Phantom Design and Construction

Figure 11 shows the setup and corresponding MR images for the initial signal test as well as CT images of the finalist materials used in the CT contrast analysis after machining. All urethane foam materials provided no measurable MR signal and thus were considered adequate for our purposes. Materials with densities smaller than 20

lb/ft^3 were found to be too brittle for precise machining, as the material was prone to crumbling. Materials with densities larger than 40lb/ft^3 were considered too heavy and were not included in the CT contrast analysis. CT signal of the final foam samples, and thus contrast between foam and paintball, were dependent on both the manufacturer and density with a CT signal intensity difference from background of 636, 483, 478, 769, and 592 HU for materials 1-5 respectively. Thus, in order to achieve optimal contrast and maintain the lowest reasonably achievable weight without sacrificing machinability, the 20 lbs/ft^3(D) material was used for phantom construction.

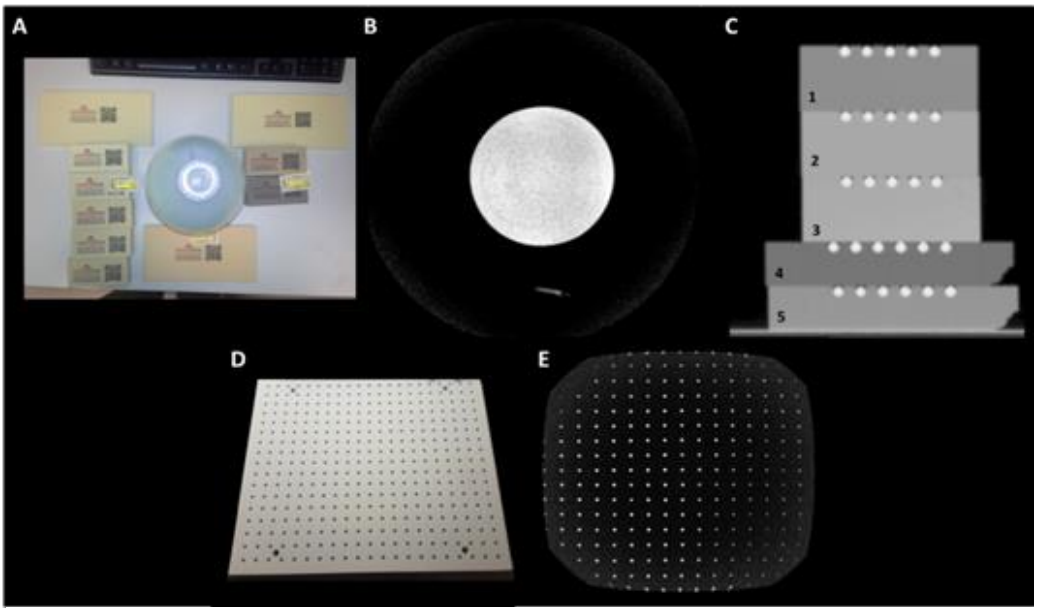

Figure 11: (A) Image setup for MR signal study. (B) corresponding MR image. (C) CT image of material finalists w/ paintballs after machining. (D) Plate from completed phantom. (E) MR image of completed plate

Figure 12 depicts various modeled bore and phantom arrangements as simulated by MATLAB. The top two rows show 60cm cylindrical bore configurations and an open bore Philips Panorama, while the bottom row illustrates widely used 70cm bore configurations. The illustrated phantom design utilizes a stack of 15 plates (2.5cm thick), and a FOV of 55x55x37.5cm (L-R, S-I, AP), and while this design works well for

the 60 cm bores, it leaves a significant portion of the FOV on the 70cm bore uncharacterized. For this reason, we chose to build the phantom using a modular design with two main configurations: (1) the standard build as shown in figure 12, and (2) the extended build, which utilizes a stack of 20 plates and a final FOV of 57.5x55x50cm (L-R, S-I, AP).

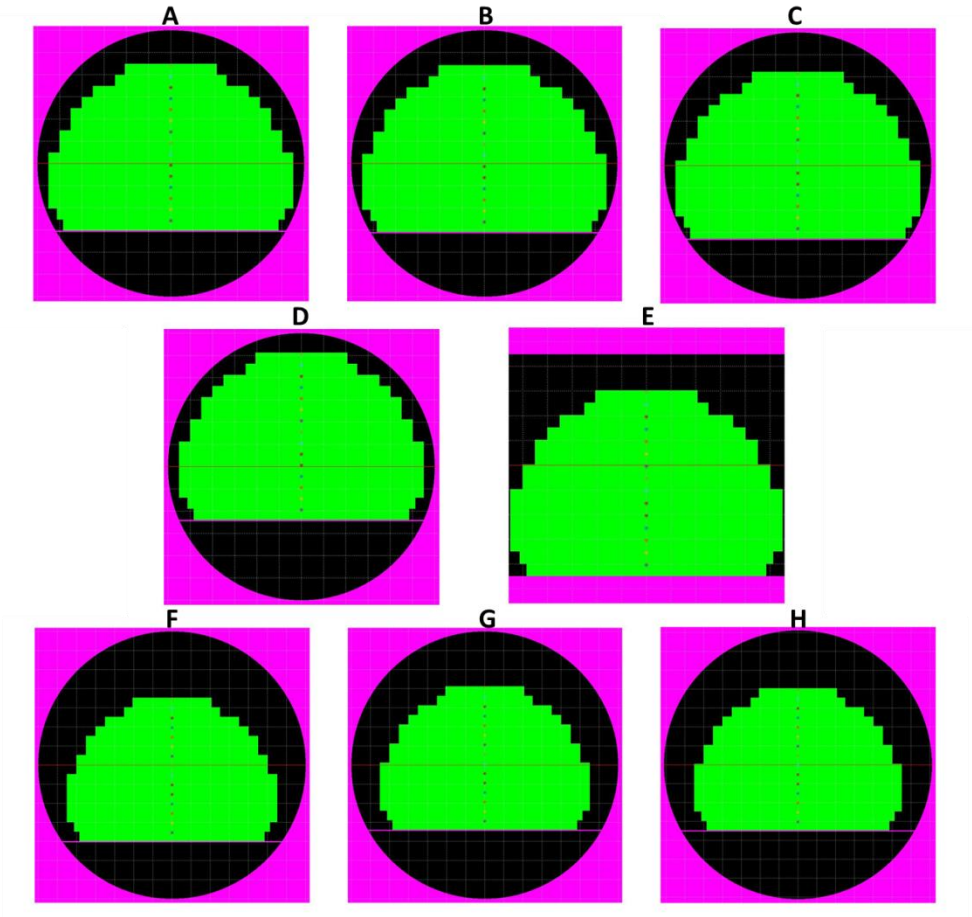

Figure 12: (A) Siemens Symphony; (B) Siemens Avanto; (C) General Electric Signa; (D) Philips Intera; (E) Philips Panorama; (F) Siemens Aera, Skyra, Verio, and Viewray MRIdian; (G) General Electric Optima, Discovery; (H) Toshiba Titan

Additional holes were drilled and fit with fiberglass tubing inserts to allow the plates to be stacked, with the plates held together using 3/8 inch diameter and 16 threads per inch fiberglass rods and hardware to secure the stack together once the

paintballs were loaded. One advantage of using this modular design was that each successive plate in the stack locks the paintballs into the plate below it.

Software Design

Figure 13 shows the graphic user interface developed for the first version of the distortion module within 3DSlicer. Utilizing previously implemented tools and existing VTK, ITK, and Qt libraries, a beta version of our distortion characterization software was integrated into the 3DSlicer tool set. By using C++ as the primary language of implementation, the total run time was approximately 8 minutes for an Intel Core i7-4770 CPU). When compared to our previous MATLAB code for a similarly sized phantom, the overall run-time efficiency gain was ~50% (17 mins for MATLAB vs. 8 minutes for Slicer3D).

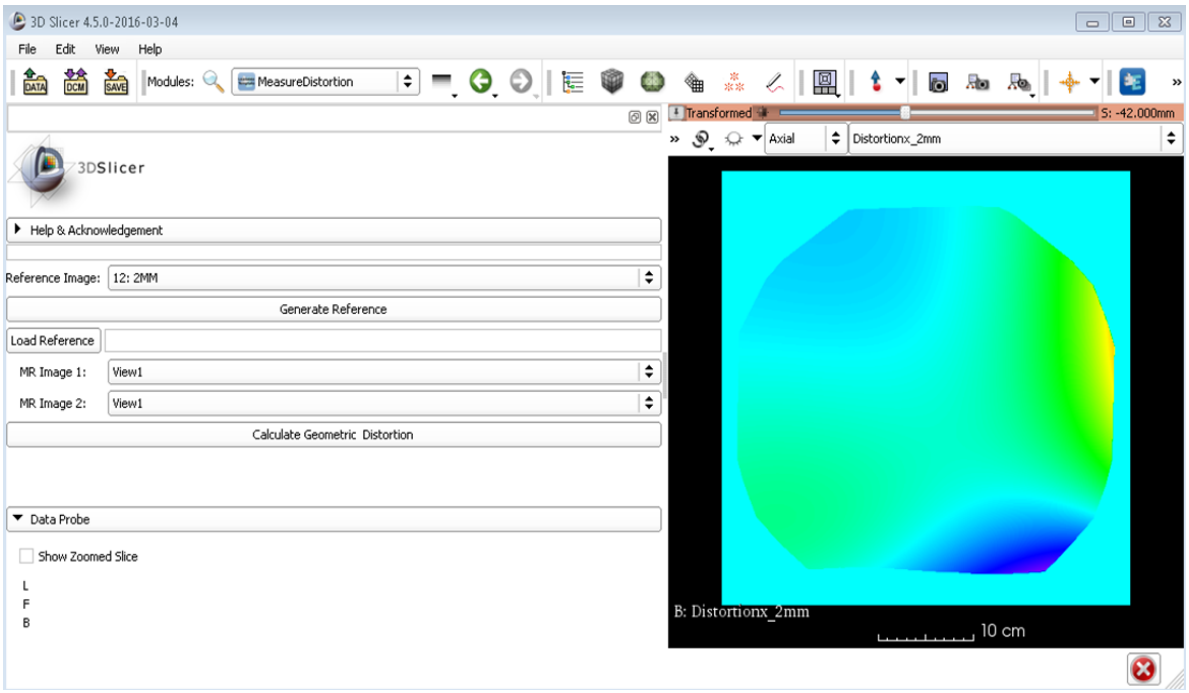

Figure 13: 3DSlicer distortion module graphic user interface

Software Validation

To evaluate the software performance, GNL was evaluated for our 1.0T HFO MR-SIM and compared against our previously published results. The plots shown in figure 14 demonstrate the distortion as a function of radial distance from isocenter in all three axes, where the top row was generated with the MATLAB software as discussed in chapter 2, and the bottom row was generated using 3D Slicer and measured using the modular distortion phantom. Both approaches measure similar distortion distributions, with the closest distortion greater than 1mm occurring at ~10cm for both the LR and AP axes. The greatest variation occurred in the SI direction, where the closest distortion >1mm occurred at ~10cm for the approach utilizing the original phantom and MATLAB, but occurred closer to 5cm for the approach utilizing the modular phantom and Slicer.

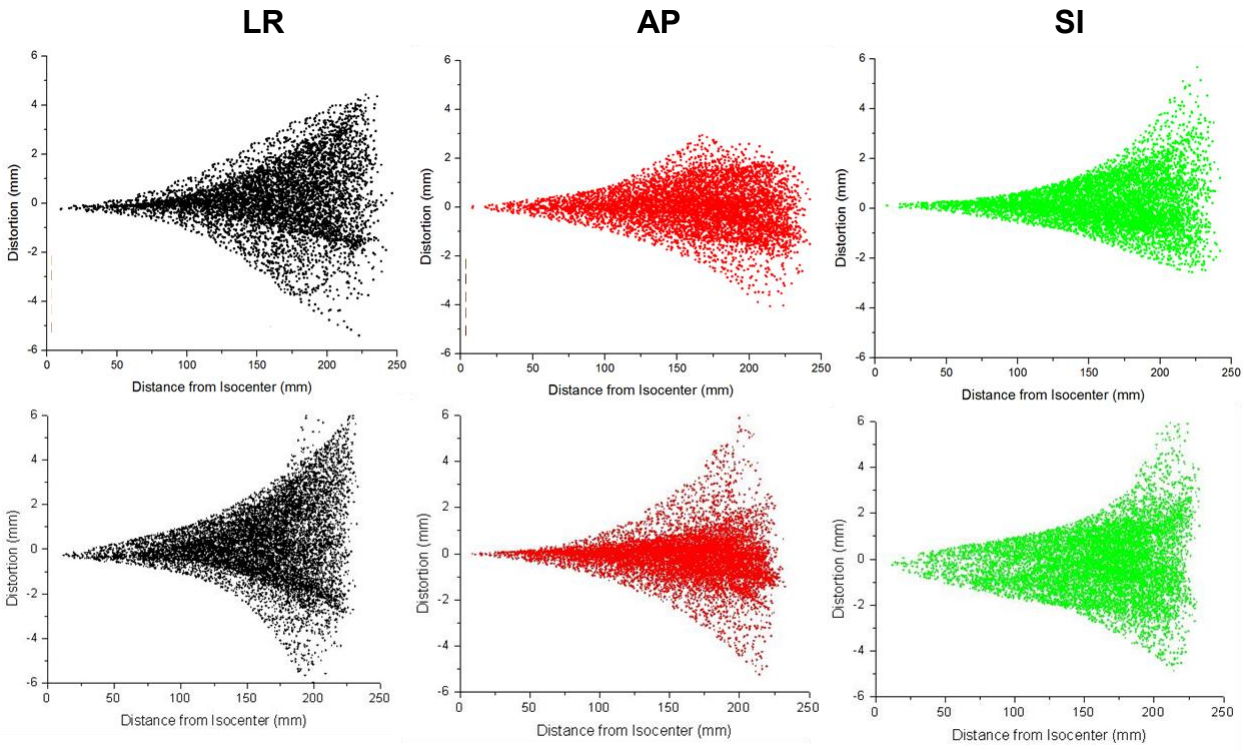

Figure 14: (Top Row) Distortion plotted as a function of radial distance from isocenter as generated with MATLAB software discussed in chapter 2 for the LR, AP, and SI distortion from left to right respectively. (Bottom Row) Similar distortion maps as measured with the new phantom and generated with 3D Slicer.

Table 4 summarizes the statistics for these distortion maps, and overall both the MATLAB/Phantom (methods 1) and Slicer/Modular Phantom GNL distortion measurements (methods 2) show similar results. Methods 1 measure more than 1mm of distortion in the L-R direction for over 39% of voxels, while the methods 2 measure similar distortion for over 45% of voxels. Similarly for the A-P direction, methods 1 and 2 measure more than 1mm of distortion for over 26% and 22% of voxels respectively. The S-I axis, on the other hand shows significantly more distortion for the methods 2, with roughly 45% of voxels distorted more than 1mm, while methods 1 measured about 25%. Finally, the polynomial fit was equivalent for both methods, with mean absolute errors between measured distortions and the modeled distortions being less than 0.1mm different between methods.

	Original (Methods 1)			New (Methods 2)		
	L-R	A-P	S-I	L-R	A-P	S-I
Max Distortion	5.5mm	4.2mm	6.1mm	8.2mm	6.5 mm	8.7mm
Pct of voxels distorted >1mm	39.3%	26.1%	25.2%	45.6%	22.8%	45.1%
Pct of voxels distorted >2mm	14.8%	3.2%	5%	20.0%	5.9%	12.8%
Pct of voxels distorted >3mm	4.4%	0.4%	1.2%	7.8%	2.2%	3.1%
Pct of voxels distorted >4mm	0.5%	<0.1%	0.3%	2.7%	0.8%	1.0%
Pct of voxels distorted >5mm	<0.1%	0	<0.1%	0.7%	0.2%	0.3%
Mean Absolute Error	0.3+/-0.4mm	0.2+/-0.2mm	0.5+/-0.6mm	0.3+/-0.4mm	0.3+/-0.3mm	0.6+/-0.6mm

Table 4: Comparison of statistics generated for the 1T Panorama using the old phantom and MATLAB software as described in Ch 2 for methods 1, and the modular phantom with Slicer software for methods 2.

Multi-magnet Characterization

Figure 15 shows phantom setup in 3 of the magnets utilized in this study. The standard build of 15 plates (FOV of 55x55x37.5cm) was used to characterize the 1.0T Panorama (Figure 15 A-C), and the 1.5T Ingenia (Figure 15 D-F). For the 3.0T Ingenia wide bore, on the other hand, (Figure 15 G-I) an extended build of 17 plates (FOV of 55x55x45cm) was used.

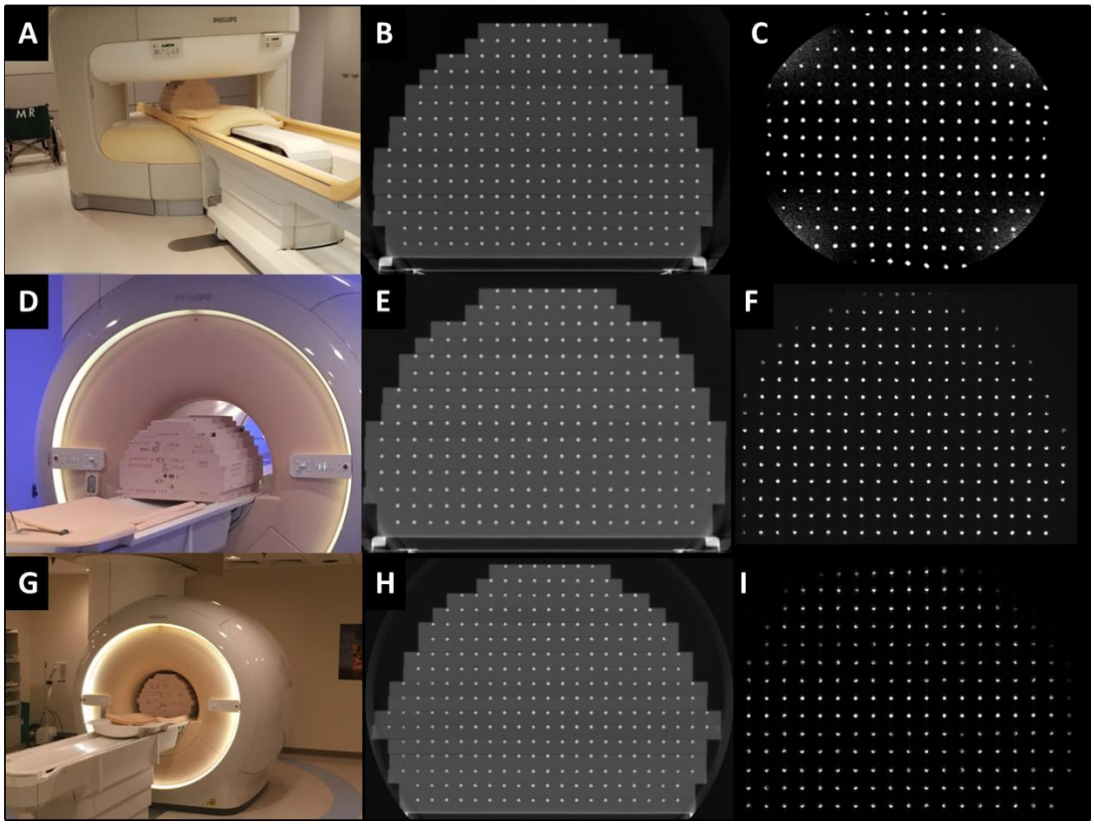

Figure 15: (A) Standard phantom setup(15 plates) on the 1T Philips Panorama with corresponding (B) CT image and (C) MR image, as well as the (D-F) standard setup(15 plates) for the 1.5T Philips Ingenia, and (G-I) a large setup (17 plates) for the 3.0T Philips Ingenia

Figure 16 summarizes the characterized GNL distortion distribution for the three MRI systems using data generated from 3DSlicer, and grouped into 3 radial distances from isocenter (0 to 10 cm, 10 to 20 cm, and > 20 cm). In general, both cylindrical bore systems revealed less GNL distortion than the 1.0 T Panorama and, although

distortions > 1 mm exist at FOV larger than 10-15cm. All systems had less than 1mm of distortion for radii less than 100 mm from the magnet isocenter, and started to deviate at distances above this for both the LR and SI directions. However, for the AP axis, both cylindrical bore systems nearly maintained less than 1 mm of distortion for the

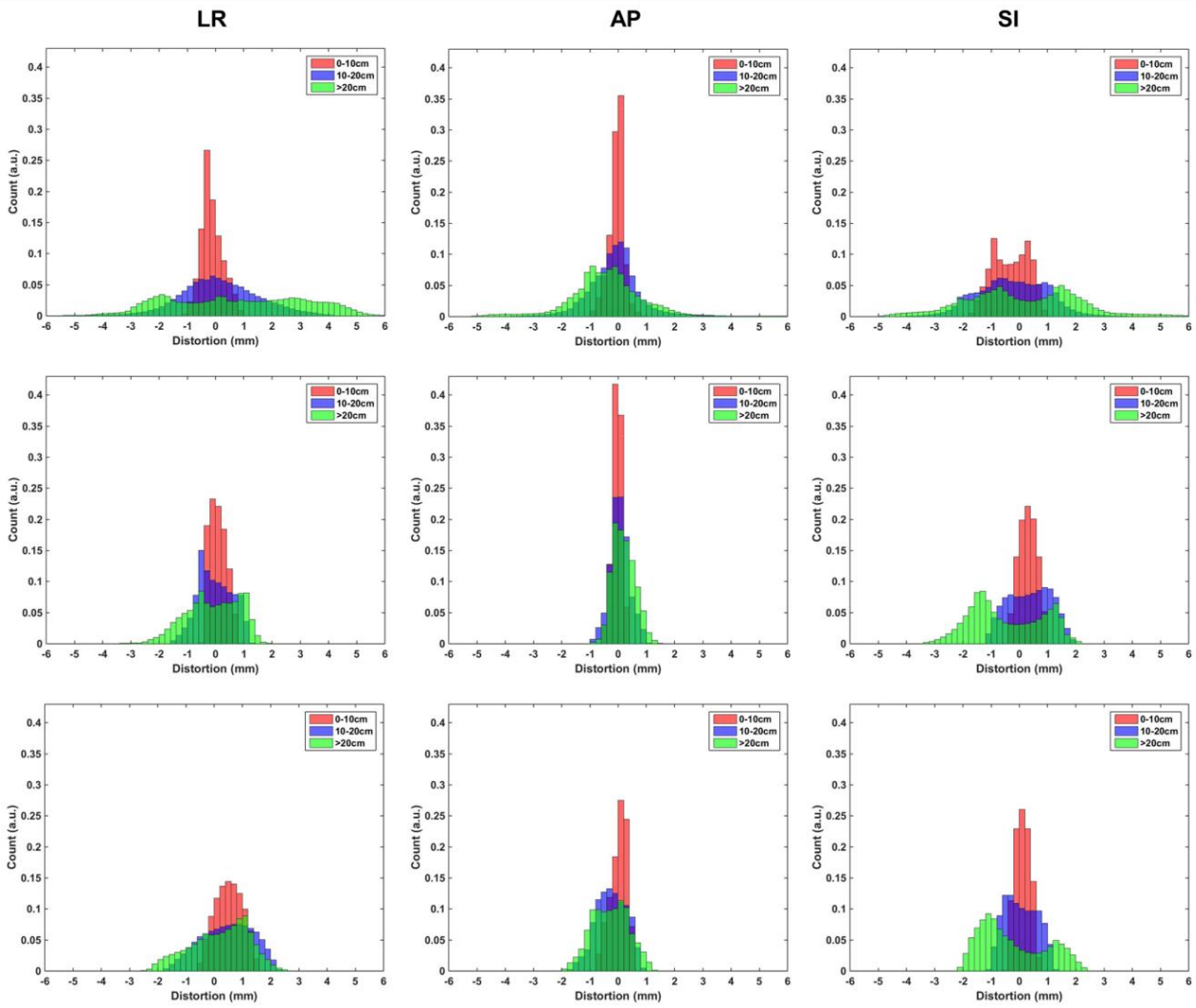

Figure 16: Histograms representing the distributions of distortion measurements for the left-right (LR), anterior-posterior (AP), and superior-inferior (SI) directions using distance to isocenter groupings. Data are shown as follows: (Top Row) 1.0 T Panorama, (Middle Row) 1.5 T Ingenia, and (Bottom Row) 3.0T Ingenia Wide Bore.

While the 1T Panorama yielded more than 1mm of distortion in the L-R direction for over 45% of voxels, the 1.5T Ingenia yielded this magnitude of distortion for about 21% of voxels, and the 3T for roughly 39% of voxels. Both cylindrical bore magnets perform even better in the A-P direction, with 1.4% and 12.6% of voxels respectively for the 1.5T and 3T, and with no voxels yielding distortions over 2mm. The differences in the amount of distortion for the S-I axis are less apparent, however the maximum distortion for the two cylindrical bore magnets are less than half of those seen on the open-bore magnet.

Discussion and Conclusion

This work sought to design, optimize and build a modular 3D large FOV distortion phantom and implement GNL distortion characterization in a widely available software platform. One key difference between the phantom designed in this work and many others presented in the literature is the modular design which allows the flexibility to custom tailor the phantom shape in order to characterize many different MR and MR-IGRT systems. Early designs, such as the phantom used by Breeuwer *et al*., focused on small regions of interest near isocenter, and thus didn't characterize distortion at the periphery of the FOV [51]. Several other phantoms do not extend to cover the entire FOV needed for MR-only treatment planning, particularly for wide-bore configurations[50, 63, 77]. Huang *et al.* limited their phantom build in the S-I dimension to reduce the weight [52], although the entire FOV could be sampled by stepping the phantom through various couch positions within the bore as described in our previous work [62].

One limitation of our phantom design is the large weight. While the phantom can be disassembled if desired for portability, the extended build utilizing all 20 plates

weighed a total of ~44 kg and required 2 staff members to assist with phantom setup. However, it is likely that after initial characterization, full FOV distortion measurements would not frequently be required as our previous work showed that the GNL distortion was stable over > 6 months of characterization [62] Recently, annual large FOV distortion measurements were recommended in the literature [30]. An alternative phantom build would be to use lighter density foam as done in previous iterations of this design; however, previous generations were also prone to damage, which can be problematic for maintaining the geometric integrity of the phantom. Another option would be to build the phantom with a shortened S-I extent, similar to Huang *et al.*, and to step the phantom to cover the entire FOV [52]. A significant challenge when building the phantom was the time required to precision machine the polyurethane foam to accommodate ~7,500 paintball landmarks. Other prototypes of similar phantoms contained a more variable density sampling pattern that would reduce the amount of machining and paintballs required, with decreased landmarks near the center of the phantom where distortions are minimal and increased number of landmarks near the periphery where more fine sampling is needed [78, 83]. Our modular phantom design provides the option of filling only some of the control points with paintballs as needed. Because the phantom required variable plate widths to accommodate the tapered design, the machining template required multiple modifications during the phantom generation. In addition, the thickness tolerance of the polyurethane foam plates was quite variable requiring additional machining to bring the plate thickness to the specified tolerance. Finally, the paintballs rest inside the drilled holes without any affixing glue, and while they are flush

with each plate surface, they often became dislodged and required reseating when phantom configuration changes are made.

The software validation shows nearly equivalent results for distortion in all axes between the old methods (stepped phantom with MATLAB software) and the new methods (large modular phantom with C++ software). The new methods measure distortions of less than 1mm up to about 10cm from isocenter both the L-R and A-P directions, with distortion increasing non-linearly as radius increases, which are consistent with previous results.[62] The S-I direction however, shows more distortion and a wider distribution for the new methods. This could possibly be the result of additional uncertainties introduced by stepping the phantom in the S-I direction. While this methodology should be accurate within 1mm, this could account for the magnitude of differences measured from our data.

As was suggested by Wang et al, the multi-magnet distortion characterization demonstrated significantly worse distortions for the open-bore 1T MRI than for either cylindrical bore magnet.[49] However, even though all images were taken with 3D distortion corrections turned on, all three MR systems experience distortions over 1mm at radii greater than 10 cm for at least 2 axes. These measurements are consistent with a recent study comparing the total distortion for multiple magnets and vendors.[63] Also, for both our study and Walker *et al* the remaining distortion post-correction for the cylindrical bore magnets increases very gradually with increasing radius, with maximum distortions (near 20cm from isocenter) of 2 to 3 mm.[63] As all scans in our setup were taken with the shutter turned off, our characterized radius was larger and thus the overall maximum distortions were larger for our setup. The A-P distortions, however

were much smaller for the cylindrical bore magnets, and, for the 1.5T Ingenia, were smaller than 1mm for nearly the entire FOV. Additionally, the increased distortion in the through plane direction (S-I) for the cylindrical bore magnets is also reported in a recent study by Torfeh *et al.*, possibly resulting from differences in gradient design for this axis. It is also worth noting that the data shown in figure 16 for the Panorama does not cover as large of a radius as the other bores. This is due to a smaller usable FOV of this open bore design in the S-I direction[84].

While the current version of the software developed for this study is limited to automated distortion characterization for our specific phantom design, it creates necessary tools for semi-automated distortion characterization on other phantoms utilizing point-like landmarks, allowing for potential widespread implementation into the community. However, before the module is made publically available it is important to first implement a robust verification and validation of the code for different hardware and software configurations. It is the goal of the coauthors to use an approach similar to that described in a previous study by Pinter *et al.,* which developed an extensive RT toolkit for 3D Slicer that was made widely available to the RT community.[85] Notable validation steps were performed including using the CTest[86] test system to perform nightly tests using reference input data and automatically comparing these results to a baseline solution. Future work will also include developing and implementing modules for synCT generation and patient-specific distortion into the same 3DSlicer toolkit.

We optimized the design and implementation of a modular, extendable distortion phantom to support an MR-only workflow and MR-IGRT. A modular phantom design was deemed necessary for large FOV distortion characterization to accommodate a

wide range of bore sizes and configurations. The phantom and accompanying analysis software will be widely available through online libraries, which will help to facilitate collaboration and multi-institutional trials for MR-only treatment planning.

CHAPTER 4 "MRI AND IMAGE GUIDED RADIATION THERAPY USING SYNTHETIC CT IN BRAIN CANCER"

Introduction

RT treatment outcomes rely on the assumption that radiation is delivered to the planning target volume (PTV) within the expected uncertainties. However, small changes in patient position, patient motion, and anatomical changes over the course of treatment can prevent accurate delivery of the intended dose.[87] In addition, dose escalation has been shown to improve local control and patient quality of life[88-90]. However, the need for accurate localization of the target becomes even more critical when using high dose gradients, such as with IMRT, or delivering high doses per fraction (i.e. with stereotactic radiosurgery (SRS) or stereotactic body RT (SBRT)).[91, 92] Currently, many modern linear accelerators are equipped for image-guided radiation therapy (IGRT) with integrated imaging systems such as cone beam CT (CBCT) and orthogonal planar x-ray imaging to enable assessment of organ motion and evaluation of patient setup error relative to the initial reference CT-SIM image. Typically patient shifts are derived by registration of landmarks or bony anatomy in the CBCT with that from the CT-SIM image, or by registration of orthogonal planar images with CT-SIM derived digitally reconstructed radiographs (DRRs). However, these methods are predicated on the assumption that CT-SIM data is available to be used for reference data.

For MR-only planning, it is necessary to generate a CT-like dataset from the MR images. Several groups,[33, 55-59] including ours,[53, 54] have developed methods for generating synthetic CTs (i.e. synCT or pseudo CT), to support an MR-only treatment planning workflow. Johansson et al. developed automatic synCT generation for the

brain using Gaussian mixture regression modeling with UTE imaging.[56] Hsu *et al* also utilized UTE imaging along with several other MR images and classified tissues based on a fuzzy c-means clustering algorithm, and assigned attenuation properties with weights based on a probabilistic model.[33] More recently, Andreasen et al. demonstrated a patch-based synthetic CT solution that uses a nearest-neighbor intensity search on a multi-patient database of MRI "patches" to assign HU values,[55] while Sjolund et al. used registration and an atlas-based database[58]. The dosimetric differences resulting from use of synCTs were also calculated within several studies.[54, 55, 57, 60, 93, 94] Kim *et al* and Korhonen *et al* demonstrated clinically negligible dosimetric differences(<2% for PTV metrics) in the prostate,[57, 60] and several groups have demonstrated similar results in the brain.[54, 55, 93, 94]

While agreement with CT-SIM and dosimetric comparisons have been explored, it is not currently known how robust synCTs are when used as the reference datasets for linac-based IGRT in an MR-only workflow. Qualitative evaluation of DRRs derived from MRI data has shown promise[33]. A patch-based "pseudo-CT" solution for pelvis in both volumetric and planar registrations for 15 patients was evaluated and differences between the pseudo-CT and CT-derived registrations were <1.2mm for volumetric and 0.3mm for planar, omitting major outliers[94]. A recent IGRT evaluation of a similar solution in brain for only 6 patients yielded < 1mm and 1° rotation differences between volumetric CBCT registrations[95]. Recently, Yang et al. performed planar kV and oblique ExacTrac image registrations to UTE-based synCTs of the brain in 7 patients, but did not evaluate the performance of volumetric registrations.[59] The work described in this chapter builds upon this current literature by including quantitative comparisons of

synCT and CT, benchmarking results in a novel MR-CT compatible brain phantom, including both planar and volumetric evaluations, and using multiple IGRT platforms for analysis in a cohort of brain cancer patients.

Materials and Methods

MR-CT Compatible Head Phantom

An MR-CT compatible 3D Anthropomorphic Skull Phantom (CIRS Inc, Norfolk) (Figure 18A) was first used to evaluate the overall IGRT workflow. The phantom consists of skull and spine bones made out of plastic-based tissue substitutes, soft tissues derived from water-based polymers, and a grid inside the cranium (3D matrix of 3mm diameter rods spaced 1.5cm apart) to serve as landmarks. The phantom has simulated ear canals (3mm diameter, 17mm long) and external markers for localization. While the phantom cannot provide varying tissue properties like patient data, the 3D-printed skull allowed for benchmarking of the overall IGRT accuracy and could be imaged across several IGRT platforms.

Patient Population

Twelve patients (mean age: 60.8±13.3years) undergoing brain cancer RT, of which one patient underwent two treatment courses, were consented to an IRB-approved prospective protocol for scanning with an investigational UTE/Dixon MRI sequence. Within one week of CT-SIM, all patients underwent an adjunct MR-SIM. Patients were treated (6±9 fractions, range: 1 to 28) using the Novalis TX, TrueBeam, Trilogy, or Edge (Varian Medical Systems, Palo Alto, CA) according to our standard of care using CT-SIM for treatment planning and IGRT. For two patients with >20 fractions, the first 4 fractions were evaluated, as many of the patients only were treated

with 1 fraction, and it was important to avoid disproportionate weighting of the data. All subsequent analysis was performed in an offline, retrospective manner.

CT Image Acquisition

All treatment planning CT images were acquired using a Brilliance Big Bore scanner (Philips Health Care, Cleveland, OH) with 120kVp, 284mAs, 0.814x0.814mm^2 in-plane spatial resolution, and 1 mm slice thickness. All patients were immobilized using a head frame combined with thermoplastic mask.

MRI Acquisition

MR images were acquired with a 1.0T Panorama High-Field Open Magnetic Resonance System (Philips Medical Systems, Cleveland, OH) using an 8-channel head coil. Due to the presence of the head coil, the head rest was the only immobilization device that was used during MR-SIM. Ultra-short TE/Dixon (UTE/Dixon), T1-weighted fast field echo (T1-FFE), T2-weighted turbo spin echo (T2-TSE), and fluid attenuated inversion recovery (FLAIR) images were all acquired during MR-SIM for use in our synCT pipeline as described below. A triple echo sequence combining UTE/Dixon imaging was taken with radial acquisition utilizing a triple echo sequence with either TE1/TE2/TE3=0.14/3.54/6.94ms or 0.14/2.44/4.74ms, time to repetition (TR)/α/density of angles =11.5ms/25°/75%, and field-of-view (FOV)=230-240mm in all three dimensions with 1.2~1.3mm isotropic voxel size. T1-FFE images were taken with a TR/TE/α=25ms/6.9ms/30° and voxel size=0.96/0.9602.5mm. T2-TSE images were taken with TR/TE/α=3802ms/80ms/90°, voxel size=0.68/0.68/2.5mm, and FLAIR images were taken with TR/inversion time (TI)/TE/α=11,000ms/2800ms/140ms/90°, voxel size=0.9/0.9/3mm.

As shown in chapter 3, it was found that the GNL distortions were <1mm within 10 cm of isocenter[62], and thus are negligible for this brain study. Patient-induced distortions arising from susceptibility and chemical shift have shown a dependence on field strength and can be considered negligible for low field systems.[64, 65] In addition, appropriate sequence selection (i.e. TSE sequences and high readout bandwidths[30]) minimized chemical shift and susceptibility-induced distortions (99.9% of voxels distorted less than 2.23ppm for brain scan[96], which is equivalent to <1 pixel for our image parameters and field strength).

Synthetic CT Generation

Twelve SynCTs were generated from MR-SIM datasets using a previously developed automated image processing pipeline[54]. This automated pipeline consists of three major workflows: (1) generation of a bone-enhanced image, (2) air mask segmentation, and (3) final generation of synCTs(see figure 17). Bone-enhanced images are generated via an optimal weighted combination of an inverted UTE magnitude image and water/fat maps generated from the 2-point Dixon method (which utilizes 2 echos, 1 with water and fat in phase and 1 with them out of phase, in order to determine final water/fat maps). The first step of the automated air segmentation was to perform a 3D unwrapping of the phase images using Prelude[97] in FSL (Analysis Group, FMRIB, Oxford, UK[98, 99]) which isolates the susceptibility-induced, chemical shift-related phase, and tissue conductivity-related phase zero maps via solving the set of linear equations common for multiple gradient echo image processing[100, 101]. A 6-kernel Gaussian Mixture Model (GMM) classifier is then applied to the phase zero map with patient-specific parameters estimated using the expectation maximization algorithm[102].

Morphological filtering and removal of cerebral spinal fluid (CSF) yielded the final air masks. These are inputted into a previously established synCT workflow along with the bone-enhanced, FLAIR, and UTE datasets. Images are automatically segmented using a 5-kernel GMM. A manual assignment process classifies each tissue type as air, bone, fat, brain matter, or CSF. Then, synCTs are generated using a bulk density representation for air while all other tissue types are patient-specific with intensities obtained via a voxel-based, weighted summation method from the bone-enhanced, FLAIR, and UTE images[53, 54]. Due to the reduced complexity of the phantom, the inverse UTE image and 3-kernel GMM were used for segmentation with slightly different material weightings. Since there was no obvious phase difference in the head phantom, air segmentation was performed manually for the small air volume in the ear canal.

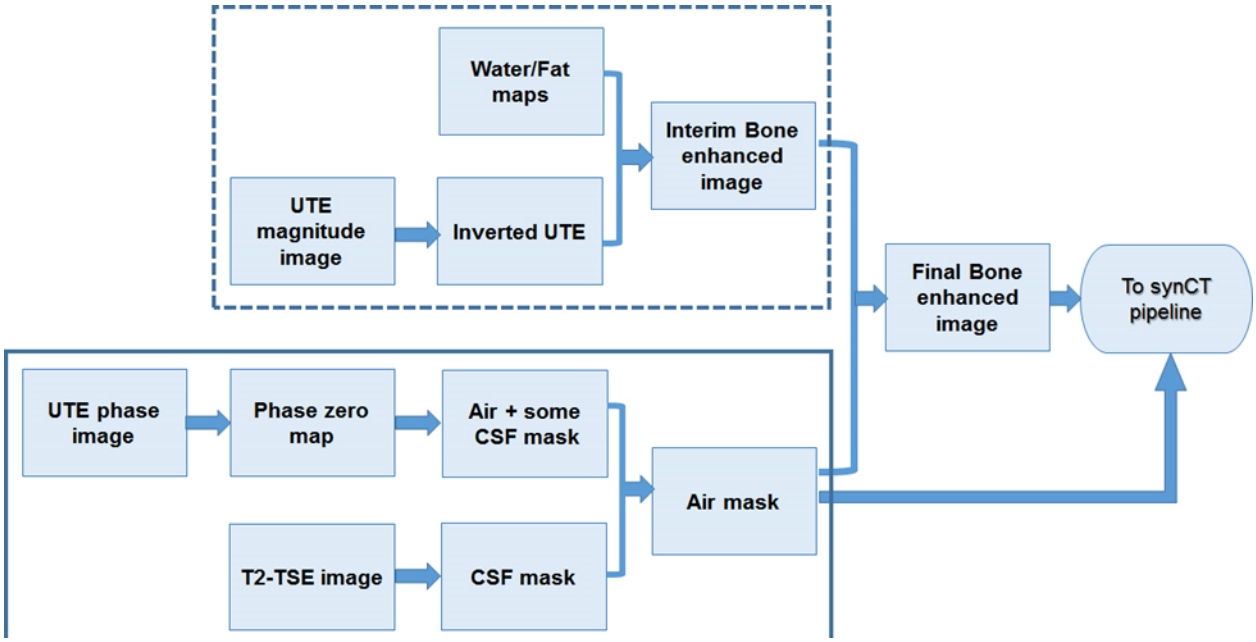

Figure 17: Previously developed automated image processing pipeline for generating synthetic CT images of the brain.[54]

To allow for spatial comparison between CTs and synCTs, CTs were then all registered to the bone-enhanced image using Elastix (University Medical Center Utrecht, Utrecht, Netherlands) with affine methods, a multi-resolution approach(4 resolution levels), and normalized mutual information (NMI) as the similarity metric. All registrations were performed with initial registration parameter settings for number of histogram bins, maximum iteration number, and number of spatial samples of32/600/10,240 for resolution level 1, 64/300/20,480 for resolution level 2, 64/300/40,960 for resolution level 3, and 64/300/122,880 for resolution level 4. A head mask was generated by thresholding the first echo of the UTE magnitude image, and applied to all MR-generated images. All images were then imported into the Eclipse Treatment Planning System (Eclipse TPS, V11.0, Varian Medical Systems, Palo Alto, California) for further evaluation, and DRR generation. SynCTs were validated by calculating the mean absolute error (MAE) between synCT and CT. Also, patient treatment plans were calculated for one patient with above average MAE and compared between CT and synCT.

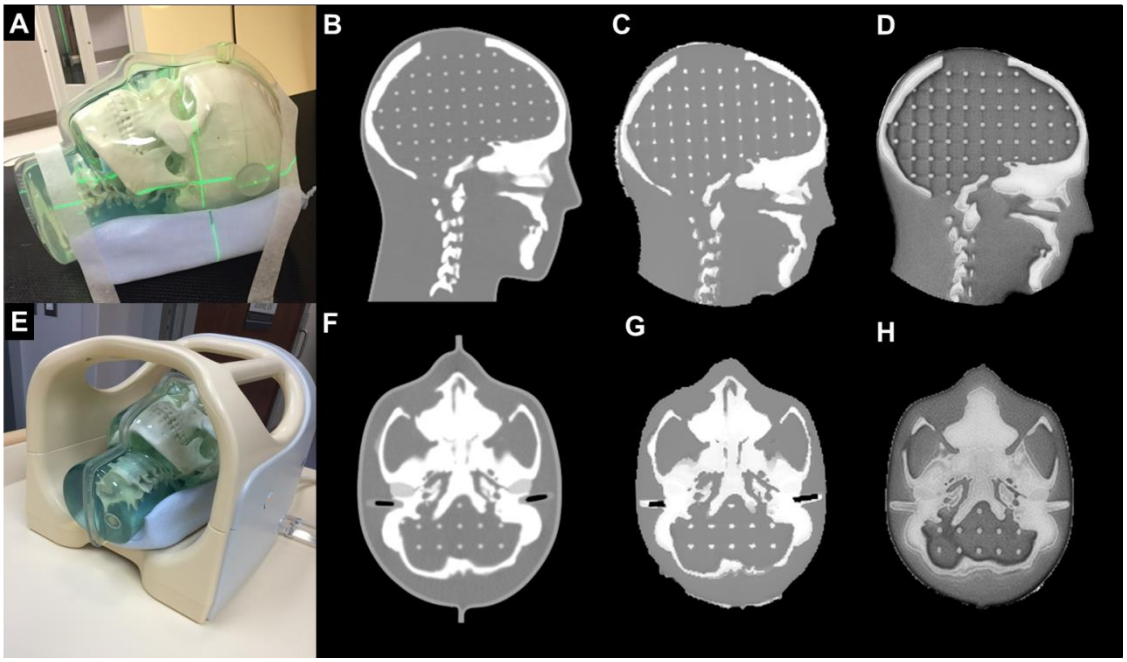

Figure 18: (A) MR-CT compatible phantom on CT-SIM table; (B) Sagittal CT; (C) Sagittal synCT; (D) Sagittal MRI (inverted UTE); (E) Phantom in 8-channel head coil on MR-SIM table; (F) Axial CT (G) Axial synCT; (H) Axial MRI (inverted UTE).

DRR Generation and Evaluation

Once the synCTs were imported into the treatment planning system, setup imaging fields from the clinical treatment plans were copied to the synCTs. For all patients and the skull phantom, DRRs were generated at all cardinal angles using fixed window settings upon export (100 to 1000 HU). To evaluate the geometric fidelity of the DRRs, a semi-automatic bounding box analysis and landmark evaluation was conducted for the skull phantom. For the bounding box analysis, DRRs were exported to MATLAB® (Mathworks, Natick, MA) via a DICOM export filter. A manually-placed box, with the inferior border set to the bottom of the cranium, was used to isolate the skull from the immobilization devices for analysis. Then, a k-means clustering algorithm with two clusters was used to segment the bone, and the resulting image was used to automatically calculate and compare the bounding box width and height. Landmark evaluation was performed by exporting all DRRs via a DICOM filter to ImageJ (available

at http://rsb.info.nih.gov/ij) for analysis. An ROI template was generated to plot a line profile through both bone and internal grid landmarks (Figure 22) at the same location for each DRR, and an automated peak-picking algorithm was used in MATLAB to find the location of local maxima of the landmarks. The peak positions of the landmarks between both DRRs were compared as a surrogate for geometric equivalence.

On-Board Image Acquisition

For the phantom, CBCT, KV, and MV images were acquired on 3 different linear accelerators (Edge, Novalis TX, TrueBeam) using clinical presets outlined in Table 3. For the patient study, an offline, retrospective evaluation was performed using available treatment positioning verification data including CBCT, kV/kV, and/or MV/kV planar imaging according to clinical protocol. Table 3 summarizes acquisition parameters and fractions used for offline registration. Verification images were exported from Eclipse TPS using an integrated DICOM filter (Image Browser, V11.0).

Linear Accelerator Platform	CBCT					AP Planar Imaging				Lateral Planar Imaging			
	kVp	mAs	In-plane Resolution (mm^2)	ST (mm)	Fx	kVp	mAs	Resolution (mm^2)	Fx	kVp	mAs	Resolution (mm^2)	Fx
TrueBeam	100	147	0.511x0.511	1	4	85	5	0.259x0.259	7	70	5	0.259x0.259	7
Trilogy	100	148	0.488x0.488	3	5	100	8	0.259x0.259	4	70	5	0.259x0.259	4
Edge	100	147 to 267	0.511x0.511 to 0.513x0.513	1	16	85	8	0.259x0.259	23	70	5	0.259x0.259	23
Novalis Tx	80 to 100	738 to 740	0.488x0.488 to 0.511x0.511	1	9	6 MV	N/A	0.261x0.261	3	70	5	0.259x0.259	3

Table 5: On-board image acquisition parameters and distribution of fractions treated for the four linear accelerator platforms.

Planar Image Registrations

Offline, retrospective 2D-2D rigid registrations were performed for both planar images/synCT DRRs and planar images/CT DRRs using an in-house developed MATLAB program with rigid registrations performed in Elastix. Semi-automatic rigid registration was performed by first interpolating planar images to the same grid as the DRRs and manually adjusting a region of interest to fit closely to the borders of the skull. Then, the shift needed to optimize the normalized mutual information metric was found by calling Elastix (University Medical Center Utrecht, Utrecht, Netherlands)[103] with a preconfigured parameter file defining the required Elastix parameters. Both orthogonal image sets were registered simultaneously with a shared superior-inferior (S-I) axis, so as to determine the translations that would optimize both the anterior-posterior (A-P) and lateral registrations. Also, each image pair was initially registered using 5 degrees of freedom ((DOF) 2 translational and 1 rotational for each projection, for a total of 3 translational and 2 rotational), but all recorded angular shifts were smaller than the inherent experimental uncertainties and thus, only 3 translational DOF were recorded. All registrations were performed using a single grid resolution, 32 histogram bins, and a maximum of 500 iterations. Adaptive stochastic gradient descent was chosen as the optimization procedure, and is recommended as a robust solution by Elastix developers.[104] To assess registration reproducibility, 10 repeat registrations were performed for a subset of 8 fractions for 5 patients (80 registrations). A new ROI was drawn for each registration to include this uncertainty in the reproducibility analysis. Registration quality was determined by visual inspection and NMI metric. Patient shifts were compared for equivalence to the clinical standard (registration between planar

images/CT DRRs) using the paired t-test, and the resulting margins were calculated via the van Herk formalism[105] (95% minimum dose to CTV in 90% of patients).

Volumetric (CBCT) Image Registrations

3D rigid registrations were performed between daily CBCT images and synCTs using the Image Registration Workspace in Eclipse. Images were manually registered before adjusting a cubic ROI around the patient skull and performing an automated registration using 3 DOF, which is consistent with our clinical protocol. Registration reproducibility was evaluated via 10 repeat registrations for a subset of 5 patients. Registration quality was determined by visual inspection, and results were compared for equivalence to the CBCT/CT registration. Margins were calculated as described for planar image registrations.

Partial Brain Image Registrations

To evaluate the performance of our synCT solution for partial brain RT, a subset of 4 patients was studied based on their performance in the full planar image registration study: a patient with the largest amount of registration uncertainty, a patient with the least amount of registration uncertainty, and 2 patients with registration uncertainty closer to the population average. Figure 19 summarizes the 6 partial brain ROIs evaluated, including anterior-superior-left, anterior-superior-right, posterior-superior-left, posterior-superior-right, posterior-inferior-left, and posterior-inferior-right. Each registration was repeated 5 times for all patients and ROIs, and mean shifts were compared for equivalence between CT and synCT. Patient 14 demonstrates the CT DRRs used in the partial brain registration study for all 4 patients.

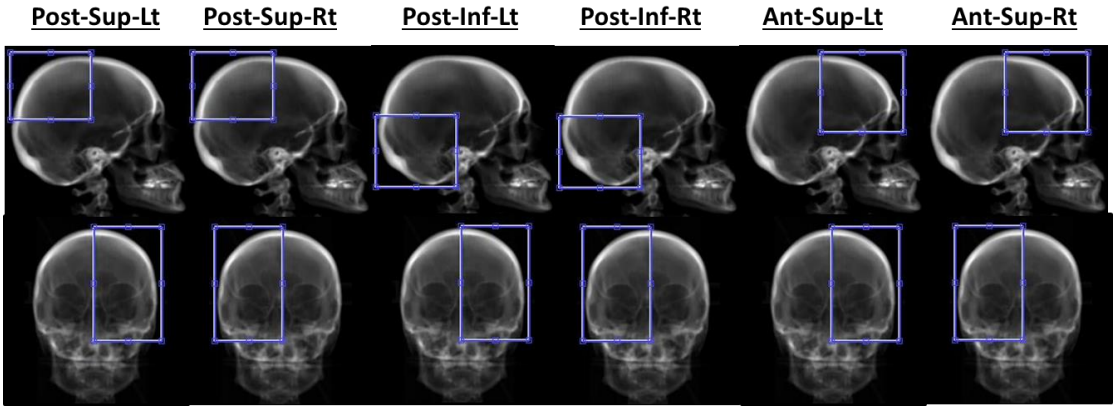

Figure 19: Six ROI pairs were used for the partial brain registration study, and included combinations of posterior-superior, posterior-inferior, anterior-superior, left, with both the left and right side of the skull.

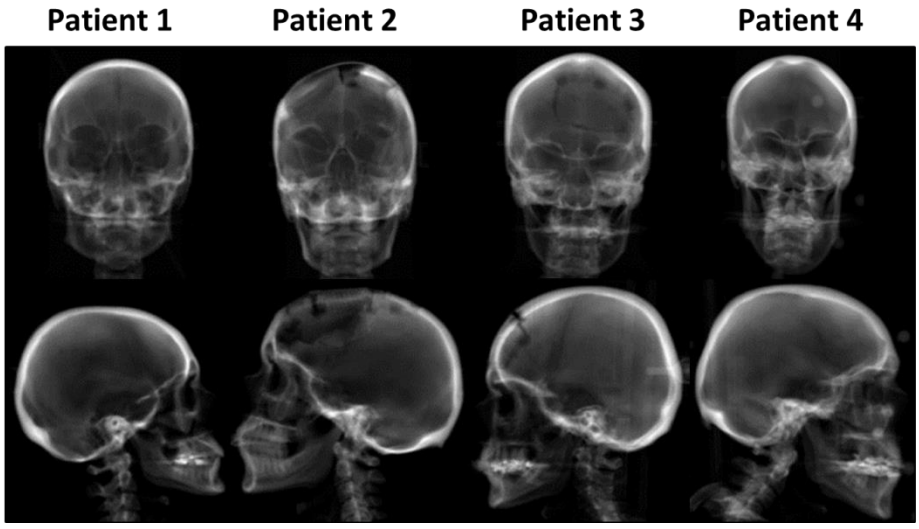

Figure 20: AP and lateral DRRs used for all four patients in the partial brain registration study

Results

SynCT MAE

The full FOV phantom MAE was 63.8 HU (bone MAE = 159.2 HU and soft tissue MAE = 17.3 HU). The patient MAE was 149.2±8.7 HU (range: 138.3-166.2 HU), with tissue MAE of 54.70±21.93 HU and bone MAE of 427.42±38.78 HU. Figure 21 shows dose planes and a dose volume histogram (DVH) for one patient case with some of the

largest differences between CT and synCT, resulting in an above average MAE. For the synCT treatment plan, the maximum dose to the PTV was 1.6 Gy smaller than for CT, while the minimum dose was 0.2 Gy smaller, and the P95 was 0.7 Gy (~2%) smaller. The max dose to each OAR was less than 0.2 Gy different between CT and synCT, except for the optic chiasm, which had a maximum dose of 13.4 Gy for the CT and 11.8 Gy for the synCT.

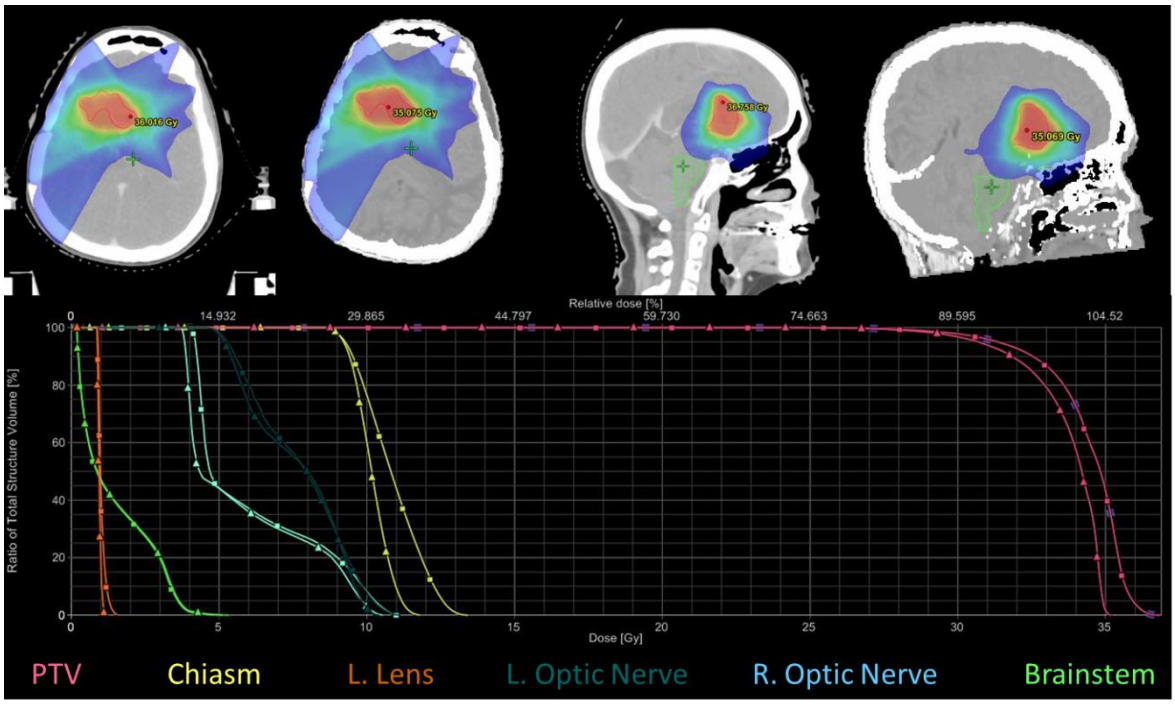

Figure 21: (Top Row) Dose plane for axial slice of CT image, axial slice of synCT image, sagittal slice of CT image, and sagittal slice of synCT image from left to right respectively. (Bottom) Comparative DVH between CT and synCT treatment plan for PTV and several OARs. Triangle icon corresponds to synCT, while square corresponds to CT.

Geometric Evaluation of Phantom DRRs

Figure 22 demonstrates the line profile comparison across phantom landmarks between the phantom CT DRRs and synCT DRRs for both right lateral and anterior projections. Overall, consistent geometry was observed between CT and synCT DRRs. The largest difference in peak-location was 1 pixel (0.98 mm) for both the A-P and the

R-L comparison. Bounding box analyses were comparable between CT and synCT: 0 and 1 mm height and width differences for A-P DRRs and 1 mm and 0 mm height and width difference, respectively, for R-L DRRs (rounded to nearest pixel). Differences in peak intensity values were observed between CT and synCT in the phantom (33±11% peak difference).

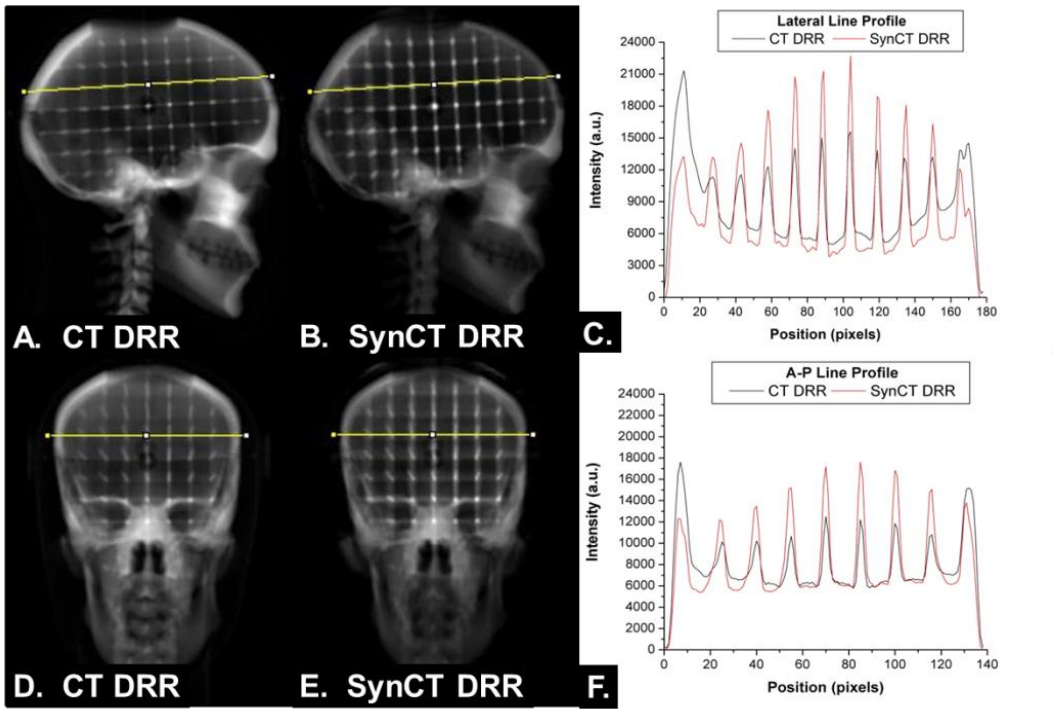

Figure 22: (A) Phantom lateral DRR generated from CT; (B) phantom lateral DRR generated from synCT; (C) image intensity profiles across the line profile for the lateral CT and synCT DRRs shown in (A) and (B); (D) AP-DRR generated from synCT; (E) AP-DRR generated from synCT; (F) image intensity profiles across line profiles shown in (D) and (E) for AP CT-DRR and synCT-DRR. Profile analysis was used for landmark evaluation to assess the synCT geometric integrity.

Phantom Registration Results

For the phantom scans, shift differences between registrations with CT-DRRs and registrations with synCT-DRRs using KV images from the Edge were 0.1, -0.1, and -0.1 mm for L-R, A-P, and S-I axes, respectively. For Novalis TX MV and KV images,

differences were -0.4, -0.1, and -0.1mm, and for TrueBeam KV images, differences were -0.2, 0.1, and 0.1mm for the L-R, A-P, and S-I axes, respectively. CBCT/CT and CBCT/synCT registrations were <0.4 mm different across all linear accelerators.

Patient Results: Planar Image Registrations

Upon visual inspection, automatic rigid registrations did not require additional manual shifts. Negligible differences in similarity metrics (NMIs) were found between rigid registration results: A-P registration yielded 0.925±0.004 (range: 0.917-0.931) for CT-SIM and 0.926±0.005 (range:0.919-0.935) for synCT. For lateral projections, NMIs were 0.917±0.009 (range:0.897-0.933) and 0.913±0.012 (range:0.885-0.927) for CT-SIM and synCT, respectively. Figure 23 shows the registration translations for the reproducibility analysis. The standard deviations (mean SD: 0.2, range of SDs: 0-0.6) depict the amount of registration variability for each subject. Figure 24(left) summarizes the distribution of translation differences between registrations performed on patient CT DRRs and synCT DRRs. The largest differences occur in the S-I axis (mean: 0.4 ± 0.5mm, range: -0.6-1.6mm). Differences in the left-right (L-R) axis were 0.0 ± 0.5mm (range: -0.9-1.2mm) and for A-P axis were 0.1 ± 0.3mm (range: -0.7-0.6mm). For the paired t-tests using an alpha of 0.05, table 6 shows there were no significant differences between CT and synCT registration for both the A-P and L-R axis with p-values of 0.58 and 0.15 respectively. However, the registration differences in the S-I axis were found to be statistically significant with a p-value of 1.21×10^{-4}. Nonetheless, the calculated synCT margins were equivalent to margins derived from CT-SIM reference datasets for all three axes, within experimental uncertainties.

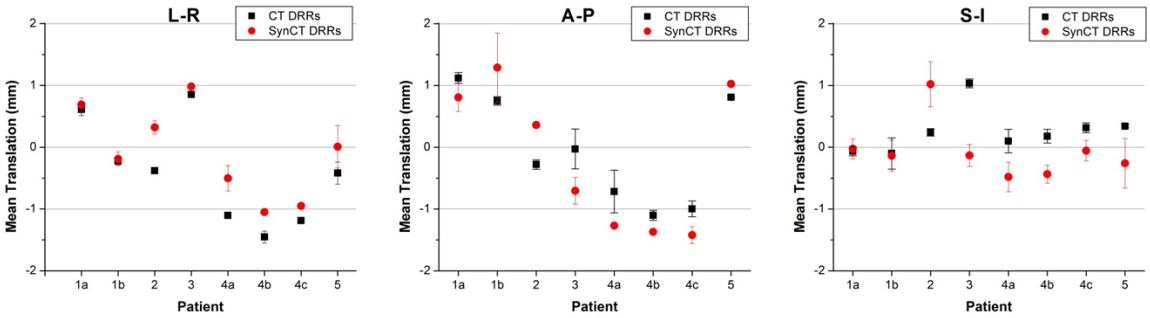

Figure 23: Planar image registration reproducibility assessment of an in-house image registration program for 5 different patients (8 fractions) using 10 repeated registrations. Mean and standard deviation of the registration translations are shown for each series.

Figure 25 illustrates DRRs for two different patients. Patient 1 yielded typical results for the population, with ~0.1mm differences in registration for both the 2D/2D and CBCT registrations and with a synCT MAE of 149.5 HU. The registrations for Patient 2, on the contrary, had the largest discrepancies between CT DRRs and synCT DRRs (~0.8mm) and synCT MAE of 140.5 HU.

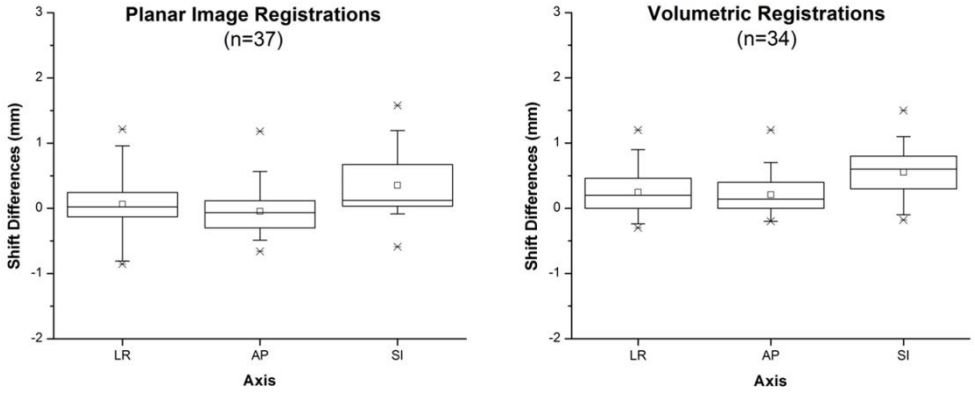

Figure 24: Distribution of registration differences obtained when synCT and CT data were used for reference datasets for the patient cohort. (Left) planar image registration differences and (right) volumetric registration shift differences. Boxplots, dotted line and circle indicate interquartile range, mean, and median respectively. Whiskers indicate 5th and 95th percentile, x's mark 1st and 99th percentile, and dashes mark the minimum and maximum shift differences. Legend: LR = left-right, AP = anterior-posterior, SI = superior-inferior

Registration	*Axis*	*Mean Difference (mm)*	*Standard Deviation*	*Standard Error*	*t*	*Degrees of Freedom*	*p-value*
Planar	L-R	0.05	0.51	0.08	0.55	36	0.58
	A-P	-0.08	0.32	0.05	-1.46	36	0.15
	S-I	0.35	0.50	0.08	4.31	36	~0
Volumetric	L-R	0.26	0.42	0.07	3.55	33	~0
	A-P	0.15	0.39	0.07	2.21	33	0.03
	S-I	0.54	0.49	0.08	6.44	33	~0

Table 6: Paired t-test statistics for the difference between registration shifts derived from CT and those derived from synCT, and the null hypothesis is that the mean difference in registration shift is equal to zero.

Patient Results: Volumetric Image Registrations

The reproducibility analysis of volumetric registrations in the patient cohort yielded an average standard deviation of 0.3 (range=0.1-0.7). Figure 24(right) summarizes the distribution of shift differences between CBCT registrations performed on patient images for the different reference datasets. The largest differences occurred in the S-I axis (mean: 0.6 ± 0.4mm, range: -0.2-1.6mm). In the L-R axis (mean: 0.2 ± 0.4mm, range: -0.3-1.2mm), and in the A-P axis (mean: 0.2 +/- 0.3mm, range: -0.2-1.2mm). For the paired t-tests using an alpha of 0.05, table 6 shows that differences between CT and synCT volumetric registration were statistically significant for all three axes, with p-values of 1.20×10^{-3}, 0.03, and 2.66×10^{-7} for the L-R, A-P, and S-I axes respectively. However, the calculated margin differences between synCT and CT-SIM reference datsets were within experimental uncertainties for all three axes.

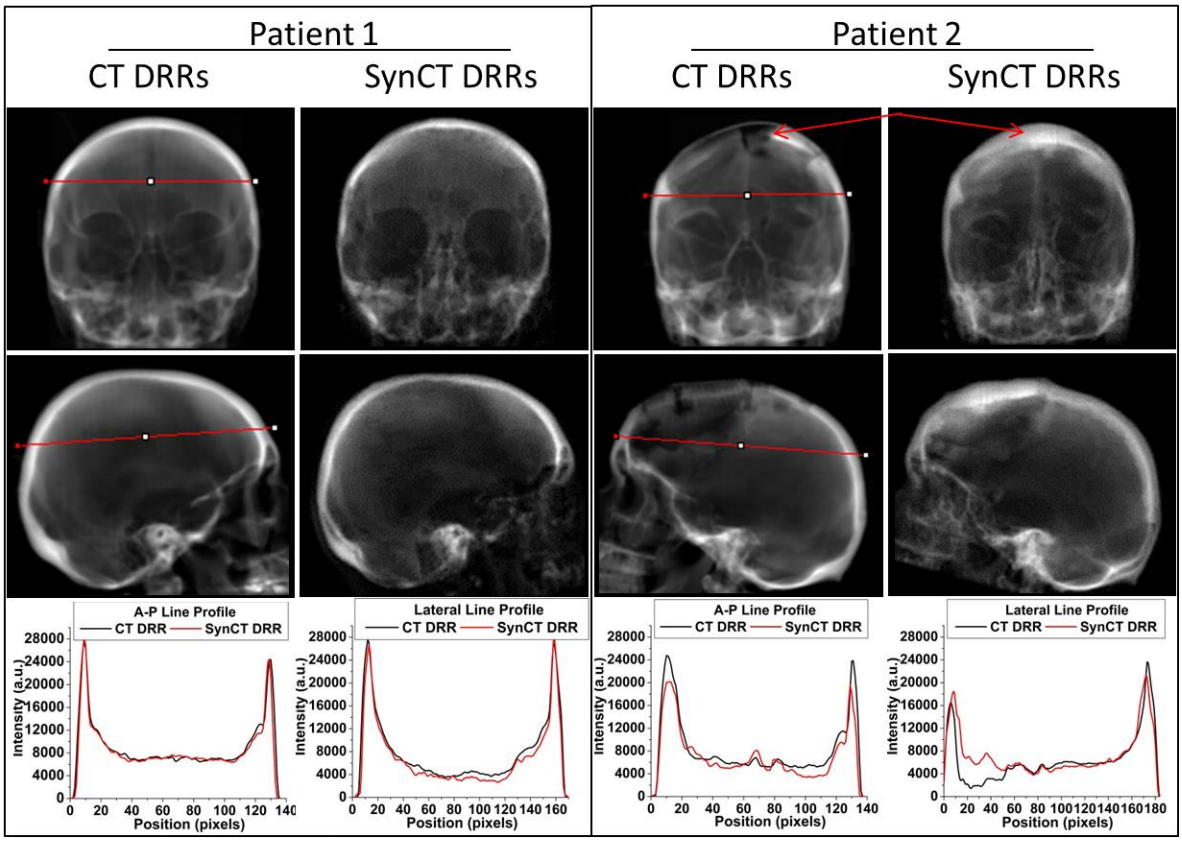

Figure 25: Anterior-posterior (top row) and lateral (middle row) CT-DRRs and synCT-DRRs with respective intensity line profiles for patients 1 and 2. Patient 1 represents typical results for the population. Patient 2 yielded the largest discrepancies in registration (~0.8 mm) due to the impact of resection on DRR quality (arrows).

Patient Results: Partial Brain Image Registrations

Table 7 shows the registration translations differences between those performed on patient CT DRRs and synCT DRRs for each ROIs for the partial brain registration study. While the largest differences occur in the S-I axis for the full brain IGRT evaluation, the largest differences for the partial brain analysis occurred in the L-R axis (mean: -0.6 ± 0.3mm, range: -2.5-1.9mm). Differences in the A-P axis were -0.4 ± 0.4mm (range: -0.4-1.9mm) and for S-I axis were 0.4 ± 0.3mm (range: -1.9-0.7mm). Among patients 2 and 3, ROIs on the right side tended to have the larger deviations between synCt and CT-SIM, however for patient 2 this was likely the result of the large

resection on the right side of the skull. The overall population means and standard deviations of the differences between CT and synCT did not illuminate any particular ROI as worse than others, and almost all remained less than 1mm.

ROI		*Patient 1 Mean± StDev, mm*	*Patient 2 Mean± StDev, mm*	*Patient 3 Mean± StDev, mm*	*Patient 4 Mean± StDev, mm*	*Population Mean± StDev, mm*
Posterior-Superior-Left	X	-0.40 ± 0.99	-0.70 ± 0.37	-0.53 ± 1.34	-1.34 ± 0.40	-0.74 ± 0.42
	Y	0.58 ± 0.48	-0.06 ± 0.51	0.64 ± 1.03	-0.11 ± 0.41	0.26 ± 0.40
	Z	-0.35 ± 1.01	-0.99 ± 1.33	0.43 ± 0.44	-0.58 ± 0.26	-0.37 ± 0.59
Posterior-Superior-Right	X	-0.41 ± 0.61	-2.47 ± 0.09	-0.58 ± 1.14	-0.30 ± 0.46	-0.94 ± 1.03
	Y	0.71 ± 0.84	0.89 ± 0.27	1.85 ± 0.66	0.67 ± 0.58	1.03 ± 0.55
	Z	-0.45 ± 0.65	-0.48 ± 0.57	-0.99 ± 0.11	-0.51 ± 0.09	-0.61 ± 0.26
Posterior-Inferior-Left	X	-0.03 ± 0.45	-0.56 ± 0.53	-1.52 ± 0.6	0.14 ± 0.83	-0.49 ± 0.75
	Y	-0.17 ± 0.52	0.17 ± 0.41	0.60 ± 0.61	0.67 ± 0.51	0.32 ± 0.39
	Z	0.45 ± 0.36	-0.03 ± 0.25	-0.11 ± 0.52	-0.69 ± 0.34	-0.09 ± 0.47
Posterior-Inferior-Right	X	-0.23 ± 0.55	-2.54 ± 0.05	1.91 ± 0.34	0.08 ± 0.37	-0.19 ± 1.83
	Y	-0.29 ± 0.35	0.31 ± 0.38	-0.37 ± 0.77	0.80 ± 0.73	0.11 ± 0.55
	Z	0.47 ± 0.28	0.13 ± 0.15	0.71 ± 0.61	-0.30 ± 0.32	0.19 ± 0.48
Anterior-Superior-Left	X	-0.27 ± 0.32	0.03 ± 0.15	-1.77 ± 0.78	0.24 ± 0.17	-0.44 ± 0.91
	Y	0.22 ± 0.11	-0.05 ± 0.07	0.26 ± 0.55	0.25 ± 0.15	0.17 ± 0.14
	Z	-0.87 ± 0.11	0.04 ± 0.13	-0.93 ± 1.40	-0.75 ± 1.37	-0.63 ± 0.45
Anterior-Superior-Right	X	-0.67 ± 0.65	-2.53 ± 0.05	0.42 ± 0.69	-0.54 ± 0.42	-0.83 ± 1.23
	Y	0.92 ± 0.59	-0.41 ± 0.06	0.27 ± 0.97	1.00 ± 0.62	0.45 ± 0.66
	Z	-0.25 ± 1.19	-0.14 ± 0.07	-1.89 ± 1.29	-1.07 ± 0.68	-0.84 ± 0.81

Table 7: Mean registration differences and standard deviations between synCT and CT reference data sets for 6 different ROIs. X corresponds to image shifts in the L-R direction, Y the S-I direction, and Z the A-P direction.

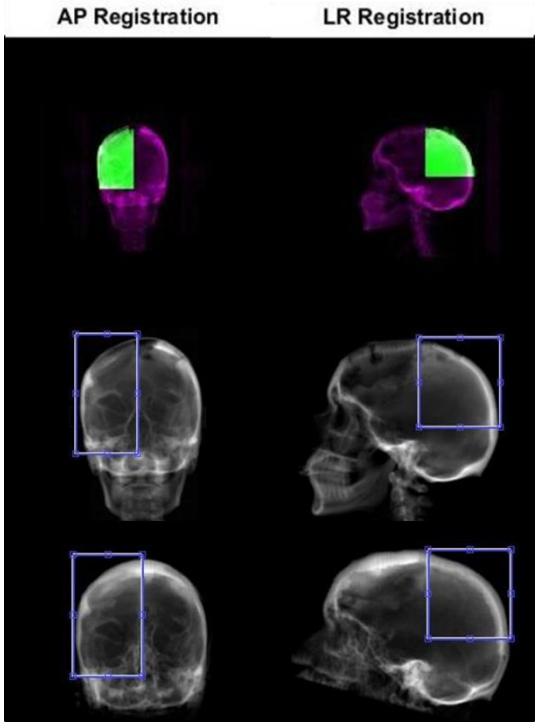

Figure 26: (Top) Registration overlays for patient 2, and corresponding (middle) A-P and lateral CT DRRs and (bottom) synCT DRRs

Discussion and Conclusion

The accuracy and reliability of conducting IGRT with synCT data have been compared to the use of CT-SIM. In the phantom, geometric DRR evaluation yielded comparable results between CT and synCT based on landmark analysis. However, slight differences in peak intensity values were observed in the phantom, whereas these were not as apparent in patient DRRs (Fig 5). This is likely due to the synCT algorithm being optimized for variable tissue contrasts present in patients as compared to the phantom. Intensity discrepancies were observed for Patient 2 near the region of the resection cavity due to misclassification. Nonetheless, the registration uncertainty for this case was <1mm between synCT and CT references. Our results are consistent with a recent comparison between 10 paired points between MR/CT DRRs, yielding a

mean difference of -0.05±0.85mm (maximum of ~2mm)[106]. Our bounding box analysis for the phantom also demonstrated differences between the overall skull geometries within this range. A limitation of using the head phantom for synCT validation is that some components (i.e. air-filled ear canals and nearby material) did not yield detectable MR signal (Fig 16H). This resulted in an inaccurate segmentation of the air cavity with some material misclassified as bone. Nevertheless, the landmarks were sufficient for analyzing the geometric integrity of synCT DRRs.

The largest patient MAE deviations were observed near the segmented bone and air regions, where the impact of misregistration and segmentation errors will contribute to higher MAEs. This also explains why the MAE for bone is much higher than for soft tissue (427 HU vs 55 HU). Also, as noted for patient 2, the intensity discrepancies present near the resection resulted in this patient having above average MAEs, while another patient (see figure 20) had increased MAE resulting from a segmentation error at the posterior portion of the skull where an anomaly occurs, resulting in the confluence of four different sinuses (as noted in Zheng *et al.*[54]) The overall MAE is consistent with the range reported in our previous feasibility study developing the synCT pipeline using fewer patients (147.5±8.3 HU)[54], as well as in the literature[56, 58]. However, as shown in figure 21, these MAEs have may have a small impact on the overall treatment plan dosimetry. The patient shown in this figure (patient 7) is shown to have an above average difference in MAE, and presents with a 5% dose difference between the point of dose max for CT and synCT. Although other studies show less minimal impact of intensity differences: Zheng *et al* demonstrated similar MAEs near air bone interfaces, and there were negligible changes in target coverage, even for the patient case with the

worst MAE (<0.5% difference for both D95 and maximum dose).[54] Also Jonsson *et al*. demonstrated maximum point dose differences of up to 1% when using bulk density overrides for synCT generation[107]. The registration reproducibility analysis showed that the magnitude of variability was patient-dependent. Two patients with the highest standard deviations in the S-I direction were found to have a partially distorted cerebrum after resection (Patients 2 and 5, Figure 25). However, the largest standard deviations were 0.6mm for 2D/2D and 0.7mm for volumetric registrations. These values are within the expected variability for automated planar [108] and volumetric CBCT registrations [109] for IGRT systems[110].

On average, patient registration differences were largest in the S-I axes (0.2mm larger on average). Similarly, the p-values calculated from the paired t-test of the 2D/2D registrations showed statistically significant differences between CT and synCT in only the S-I direction. A possible explanation for the reduced performance in this axis could be related to the slightly larger CT slice thickness (~1 mm) as compared to the in-plane resolution (0.8 mm). This could also be the result of slight errors in the positioning of the kV imaging equipment. While the simultaneous registration of both orthogonal image sets with a shared S-I axis allowed for a single optimized simulated patient shift, it has to the potential to also exacerbate any systematic differences that exist between the A-P and L-R images. These differences could potentially reduce the quality of synCT registrations in the S-I direction thus resulting in larger differences between Ct and synCT in this axis. However, the p-values from the paired t-test of the volumetric registration analysis showed statistically significant differences in all three axes, and thus under the current assumptions can reject the null hypothesis that these

registrations are statistically equivalent. One potential source of error in this study is the initial registration between CT and the bone-enhanced image. Any errors in this initial registration would propagate throughout the study, and could contribute to this result. However, the mean difference between CT and synCT was calculated to be 0.3mm, which is less than the experimental uncertainties involved in this study. Also, some of the difference between CT and synCT for the patient registrations are likely the result of anatomical differences which are not corrected by rigid registration and therefore do not entirely result from differences in synCT quality. Additionally, for both 2D/2D and volumetric registration, margins calculated for synCT were equivalent to CT for all axes. So while some of the differences measured in this study were statistically significant, they pose little potential for clinical significance for the majority of patients in this study. Patient 2 had a large piece of the skull surgically removed (Fig 5) and thus, intensity differences resulted between the CT and synCT generated DRRs in the resected area and adversely affected the synCT DRR quality. Even though these evaluations included residual uncertainty of the registrations, in this worst case scenario, the overall registration differences between CT and synCT were still within the reported registration error for IGRT systems (0.4-1.1mm)[108-110]. Additionally, the population mean difference between partial brain registrations for CT and synCT were less than 1mm different for nearly all 6 ROIs, with the largest being 1mm. Figure 26 shows the CT DRRs and synCT DRRs with an overlay of the final DRR registrations for the patient 2 and the posterior-superior-right ROI, which exhibited the largest differences between CT and synCT overall. Registrations for this patient were over 2.5mm different between CT and synCT for all 3 ROIs involving the right side of the skull near the resection cavity.

However, while this patient also had some of the largest differences in the whole-brain IGRT evaluation, it maintained less than 1mm difference between CT and synCT. This suggests that when using synCT for IGRT in areas of large resection cavities, it would be advantageous to consider whole-brain localization as opposed to localized registration near the resection cavity. Improvements of the synCT algorithm are needed in areas of large resection, where the cavity is sometimes characterized as bone instead of soft tissue or edema.[54] Also, as mentioned above this study is limited in that the comparison of these registration shifts rely on accurate initial registration of the CT images into the MR coordinate system. Any errors introduced in this preprocessing step would be systematic, and propagate into the 2D/2D and volumetric registration studies, potentially impacting results. However, this step is necessary to conduct a simulated patient setup comparison between both modalities, and was used by other similar studies in the literature.[59, 95]

Yin *et al.* showed that MR-DRRs and CT-DRRs were within 2.5mm in a phantom and patient case using Chamfer matching[111] although the MRI acquisition was not optimized for MR-simulation (i.e. 5mm slice thickness, 2.5mm slice spacing). Using thinner slice thicknesses is a key component to generating accurate DRRs. During our initial synCT brain algorithm development, we highlighted 2 out of 10 cases that required modified air masks in the frontal sinus region via an additional post-processing step using the UTE magnitude image and morphological erosion[62]. This modification increased the true positive rate (TPR) agreement with CT-SIM air segmentation by 2 and 5% for the 2 patients. However, applying this technique for the rest of the cohort did not change their TPR results (<0.1% different). In the whole-brain IGRT evaluation,

rigid registrations were performed using the entire cranium whereas in partial brain RT, local registrations could be performed in regions with higher uncertainty that may influence registration performance. For example, if a localized portion near the frontal sinus were used where uncertainty may be greater, caution would need to be exercised to ensure accurate synCT geometry. Recently, oblique ExacTrac brain images were registered to UTE-based synCTs in 7 patients and registrations were <1mm/1° different.[59] Our typical patient results were consistent with this work as well as another by Edmund et al[95], with 17 out of 18 of our population mean registration differences being less than 1mm. Our study additionally presented a worst case scenario in an attempt to characterize the upper limit of registration performance in this setting, and it was shown that this patient exhibited up to 2.5mm of registration difference between CT and synCT. However, this study only involved 4 patients and may not represent accurate population statistics, and a larger study is warranted.

To translate to other field strengths, UTE-Dixon acquisition parameters would need to be optimized and post-processing corrections for bias field and patient-specific distortions would be required. Putting our findings into clinical context, the recommended CTV to PTV margins for IMRT range from 3-5mm for glioblastomas[112], and thus, our registration errors using synCTs as the reference dataset were within a clinically acceptable range (i.e. <0.3mm difference in margin calculation). Previously, we found that synCT plan quality met all clinical criteria with no systematic differences when used as the primary treatment planning dataset[60]. These data, when taken in concert with the IGRT study, suggest that MR-only treatment planning is feasible for select partial brain RT patients. One recent study suggests that the level of MR-only

accuracy in the brain is sufficient for stereotactic applications.[59] Several groups have conducted end-to-end testing of an MR-only workflow[113, 114] and clinical studies are currently underway.

Using a previously developed synCT methodology, we have quantified the accuracy of using synCT in an IGRT pipeline relative to CT, which is currently the clinical standard for brain. For typical cases, the characterized differences between the use of synCT and CT were within the expected errors associated with image registration. A prospective clinical trial is warranted to determine potential gains of MR-only treatment planning.

CHAPTER 5 "CONCLUSIONS AND FUTURE WORK"

Summary of Findings

This body of work sought to address some of the major challenges that exist in implementing MR-only RTP. Specifically, we focused on characterizing some of the remaining unknown inaccuracies, while also laying the groundwork for further integration of methods into the MR-SIM workflow.

The first aim of this study focused on the technical characterization of gradient non-linearity induced distortion for large FOVs in a clinically available MR-SIM system. Using in-house developed software, this study first characterized the distortion at all three major planes through isocenter. We demonstrated that eddy currents were appropriately compensated for, and resulted in negligible variation in distortion measurements. It was also shown that this system experiences non-negligible distortions, even after applying vendor-supplied distortion corrections. However, the 2D phantom was used weekly over the course of 18 months, and the GNL distortions were shown to be consistent to baseline measurements over this entire period. This supports the implementation of annual GNL distortion measurements for routine quality assurance. This study also investigated the potential of using the 2D phantom to characterize the entire 3D field of view by stepping the phantom through the bore while scanning at various positions. It was shown that while this methodology was effective for in-plane distortion for the majority of the FOV, the distortion in the S-I direction was not improved. Finally, we used a novel, large 3D distortion phantom to characterize the distortion across the entire FOV, and demonstrated post processing correction scheme. Overall, through the characterization and correction of GNL, distortions were reduced to

<1mm across the entire FOV. This work is significant in that the community is currently lacking guidelines on MR-SIM QA and the frequency of which to measure MRI parameters. A Task Group has been recently formed to address this and generate consensus statements on QA approaches and suggested tolerances.

The second aim covered in Chapter 2 focused on the design and construction of a large FOV modular distortion phantom that has been optimized to accommodate the clinically available MR systems. In addition, we developed open-source distortion correction software for quantifying the total and GNL distortions. In this study, we first tested a set of urethane foam based materials with a wide range of densities for machinability as well as CT and MR signal relative to signal generating paintballs used as landmarks. Several of the low density materials were found to be too brittle for high precision machining purposes, and ultimately, a material with 20 lbs/ft^3 density was chosen as a compromise between contrast, strength, and overall weight. An in-house MATLAB script was also used to generate models of various MR bore and phantom designs in order optimize the size of the phantom for many different MR systems. The final phantom was designed with two main configurations: a standard build (of 55x55x37.5cm) to accommodate 60 cm bores, and an extended build for large bore systems (57.5x55x50cm). The modular phantom design and use of a CT reference as the baseline enables other phantom configurations when necessary. Using distortion characterization methods from aim 1, we developed platform-independent software integrated into a widely available medical imaging application, 3DSlicer. Preliminary results were presented, and phantom scans were acquired on 5 different MR systems for further software optimization and distortion characterization. This work is important

in that it provides the community with a system independent phantom and tool-set for characterization of geometric distortion, making implementation of these practices more accessible.

Lastly, aim 3 investigated the equivalence between synCT and CT in an IGRT setting by benchmarking results with a novel MR-CT compatible brain phantom and performing an analysis in a cohort of brain cancer patients across multiple IGRT platforms. In this chapter, we first demonstrated the intensity equivalence of our synCT solution with an overall MAE of 63.8 HU. DRRs generated from both CT and synCT of the head phantom were found to be geometrically equivalent with less than 1mm difference between the two for both a line profile and bounding box analysis with comparable registration results (<0.4 mm difference). SynCTs were also investigated for a cohort of brain cancer patients using both planar and volumetric registrations, and both were found to be within 1mm of CT registrations for the majority of patients. However, certain circumstances such as a patient with a large resection cavity, resulted in some cases with larger than average differences between CT and synCT. A partial brain RT sub-study was also conducted for a small cohort of patients, and the synCT was once again shown to be equivalent to CT-SIM for the average patients. However, caution must be exercised when the partial brain information is derived from areas where synCT performance is less accurate and intensity discrepancies occur, such as near large resection cavities. This work is significant as the accuracy of synCT in an IGRT pipeline not well studied, but is imperative for robust implementation of MR-SIM only.

Overall, we have characterized several inaccuracies within MR-only RTP while improving the accessibility of these methods so that they may be integrated into the MR-SIM workflow.

Limitations and Future Work

While much work has been done to characterize MRI in a radiation therapy setting, widespread implementation of MR-SIM is still limited by several additional challenges that were beyond the scope of this work. Further work could be done to improve the initial GNL vendor distortion correction with higher order spherical harmonic coefficients. This could allow the spatial integrity of MR images to be maintained without the need for additional post-processing corrections. Furthermore, this study was limited in that it focused solely on distortion resulting from GNL, and did not address other sources of distortion such as those arising from B_0-field inhomogeneity, chemical shift, and magnetic susceptibility differences. However, scanning with higher readout bandwidths[30, 65, 74] when possible has been shown to minimize these effects. It is also important to note that these effect are dependent on field strength, and thus additional corrections may be necessary for higher field strength magnets. To do this, a dual echo gradient echo pulse sequence can be used for phase mapping[65, 76] to measure an calculate these sequence-dependent distortion maps which can then be used for correction similarly to our application of GNL correction maps. Future work could include the characterization of patient-dependent distortions for our magnet, including susceptibility, for relevant regions of interest, which is an active area of research for our group and others.[64, 75, 96, 101] Specifically, due to the timeframe for MR imaging being ~30 minutes or more, there is need for a dynamic solution to patient

specific distortions that accounts for changing physiology during the scan (bladder/rectal filling, respiration states, etc).

Also, our study on the accuracy and reliability of conducting IGRT with synCT data is limited in that it focuses on only one of many synCT solutions, and further work is necessary to fully describe the potential of other synCT solutions in this setting. The results regarding additional uncertainty for our patient with a surgical resection also necessitates additional work to improve our synCT solution in the brain, while translation of this solution to other field strengths requires additional optimization of UTE-Dixon acquisition parameters and post-processing for bias field inhomogeneities. This work is also limited to the brain and male pelvis, but there are other areas of interest for MR treatment planning, including the abdomen and female pelvis.[115, 116] Also, while outside the scope of this work, there is potential for incorporation of functional information into MR treatment planning.[117] Thorough end-to-end testing is also an important piece of establishing MR-SIM. Sun *et al*. designed and implemented and anthropomorphic male pelvic phantom than can be utilized for end to end testing of prostate radiation therapy.[114] This pelvic phantom contains simulated OARs, and was scanned on an MR simulator with radiotherapy dedicated couch-top and laser positioning system. The phantom was planned with a seven-field IMRT treatment, and dose calculated using bulk electron densities. Another phantom with identical external structure, but with an internal geometric grid was used to measure geometric distortion. This study found a difference of less than 0.01% in dose to the prostate between MRI and CT based plans. Another statistical study by Korsholm *et al*. found that mean dose differences were slightly larger when comparing organs at risk (up to 4.2%).[113] They

also found that these overall results can be improved by accounting for air and bone in the synthetic CT. Considering that the expected uncertainty due to simulation is ~1mm, the setup uncertainty is 1-3mm, and output of the linear accelerator can be ~2%, these results are well within a reasonably expected range.[118, 119] Lastly, as MR-SIM achieves more widespread integration into the clinic, further prospective clinical trials are warranted to fully determine the benefits of MR-only treatment planning, and the potential gains yet to be achieved.

Altogether, MR-SIM has the potential to significantly reduce the soft tissue delineation variability for many disease sites, [9-13] while also avoiding the systematic uncertainties associated with multi-modality image registration and increasing the clinical efficiency.[21, 31-37] Yet some challenges still exist. While the measurement and correction of distortion has been explored at length, these corrections are still not readily available in the clinical setting. Also, air/bone segmentation still poses some difficulty. Methods such as those utilized in this work exist for automatic separation of bone and air in the skull[54], although for pelvic synthetic CT generation, some methods still require manual contouring[53] or other patient specific manual modification.[57] Overall, before the full scale of this potential can be realized it is necessary to establish confidence that MR-only simulation can be performed accurately.

Once these challenges have been adequately addressed, the future involvement of MR in RT could be extensive. For example, research is already being done to incorporate functional imaging into treatment planning. Dynamic contrast enhance MR imaging is being used to identify intra-prostatic lesions for dose escalation[120], and FLAIR imaging is being used to characterize functional lung so as to prioritize this tissue

for avoidance.[121] Also, several groups are currently working toward the application of MRI for in-room MR guided radiation therapy. One approach to this problem involves the use of a split 0.35T MR scanner with three Cobalt-60 heads. This allows for in room MR guidance, without interference of the MR system, and the low field would result in clinically negligible susceptibility artifacts. However, this system provides a limited dose rate, and images with low signal to noise ratio.[122] Another approach under development involves a 1.5T MR scanner combined with a linear accelerator; which, in a proof of concept study showed that with appropriate design, both the MR scanner and linear accelerator may be operated simultaneously without degradation in performance.[123] This design and several others under development[124, 125] would also allow for in room MR guidance with improved signal to noise ratio over the low-field design, although at 1.5T patient specific distortions may be more of a problem, making distortion mitigation/correction all the more important.[75]

To move toward this overall goal, this work has characterized the inaccuracies related to GNL distortion for a previously uncharacterized MR-SIM system at large FOVs, which is necessary for RTP applications of MRI. This work also established that while distortions are still non-negligible after current vendor corrections are applied, simple post-processing methods can be used to further reduce these distortions to less than 1mm for the entire field of view. Additionally, it was important to not only establish effective corrections, but to establish the previously uncharacterized temporal stability of these corrections. This work also developed methods to improve the accessibility of these distortion characterizations and corrections. We first tested the application of a more readily available 2D phantom as a surrogate for 3D distortion characterization by

stepping the table with an integrated batch script file. Later we developed and constructed a large modular distortion phantom using easily obtainable materials, and showed and constructed a large modular distortion phantom using easily obtainable materials, and used it to characterize the distortion on several widely available MR systems. To accompany this phantom, open source software was also developed for easy characterization of system-dependent distortions. Finally, while the dosimetric equivalence of synCT with CT has been well established, it was necessary to characterize any differences that may exist between synCT and CT in an IGRT setting. This work has helped to establish the geometric equivalence of these two modalities, with some caveats that have been discussed at length.

APPENDIX "DISTORTION MODEL COMPARISON"

While the use of a sixth-degree polynomial for distortion modeling has been validated in the literature,[67, 68] a similar, though smaller, experiment to the Hong *et al.* and Wang *et al.* was performed to characterize the errors of various models for our magnet. Two dimensional distortions present in our 1T open bore magnet were measured using the 2D distortion phantom as defined in Chapter 2 of this dissertation, and full distortion maps were generated for various polynomial models of order 3-9, as well as for a thin plate spline model. The closeness of fit was then evaluated by taking the difference between actual measured distortion at each control point and the distortion at the same location in the interpolated map, and both the maximum and mean absolute differences were plotted for each polynomial model (see figure 27). These plots show a similar trend for the polynomial models as demonstrated in the cited literature, with the smallest reported maximum and mean differences between the model and measured values occurring for polynomial orders 4-6, and the smallest magnitude value occurring for orders 5 and 6. Also, while the maximum differences occur at the periphery, the radius of maximum difference is similar for all orders of polynomial while the magnitude of the absolute maximum difference increases for the higher orders tested, suggesting that the tested higher order polynomials do not increase the quality of fit at the periphery. The thin plane spline model was not used, as this methodology resulted in overfitting and unreasonable distortion gradients (see figure 28). These results, in conjunction with the results reported in Hong *et al.* and Wang *et al.* support the use of a sixth-degree polynomial model for our purposes.

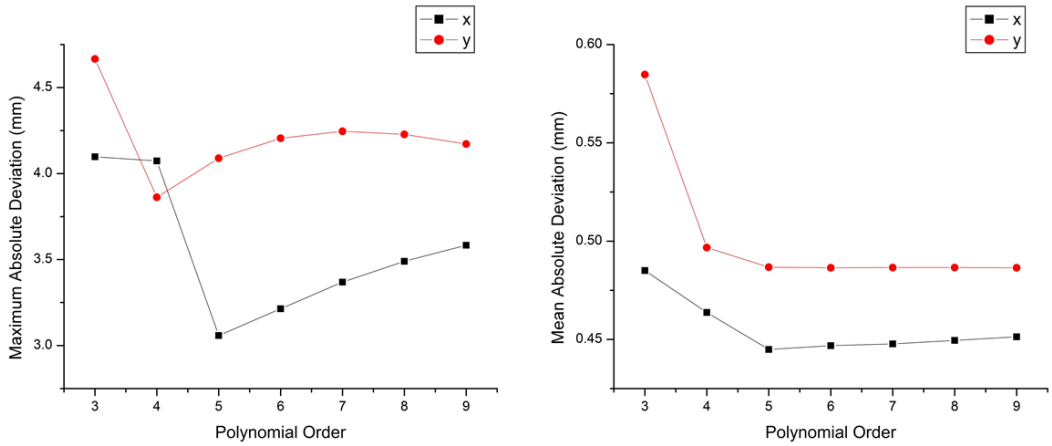

Figure 27: (Left) Maximum absolute difference and (Right) mean absolute difference between modeled distortion and measured distortion for 7 different polynomial orders.

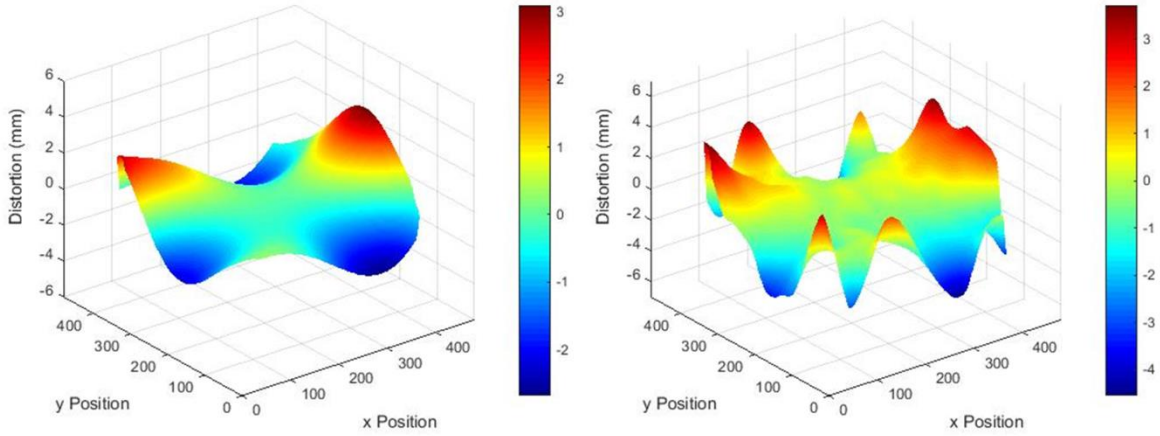

Figure 28: (Left) x-axis distortion map (mm) vs image pixel location using a sixth-degree polynomial and (Right) a thin plate spline model. The thin plate spline was found to over-fit to the data, resulting in unreasonable distortion gradients and peaks.

REFERENCES

1 U. Schneider, E. Pedroni, A. Lomax, "The calibration of CT Hounsfield units for radiotherapy treatment planning," Physics in medicine and biology **41**, 111-124 (1996).

2 C. Njeh, "Tumor delineation: The weakest link in the search for accuracy in radiotherapy," Journal of medical physics/Association of Medical Physicists of India **33**, 136 (2008).

3 E. Weiss, C.F. Hess, "The impact of gross tumor volume (GTV) and clinical target volume (CTV) definition on the total accuracy in radiotherapy theoretical aspects and practical experiences," Strahlentherapie und Onkologie : Organ der Deutschen Rontgengesellschaft ... [et al] **179**, 21-30 (2003).

4 L.F. Cazzaniga, M.A. Marinoni, A. Bossi, E. Bianchi, E. Cagna, D. Cosentino, L. Scandolaro, M. Valli, M. Frigerio, "Interphysician variability in defining the planning target volume in the irradiation of prostate and seminal vesicles," Radiotherapy and oncology : journal of the European Society for Therapeutic Radiology and Oncology **47**, 293-296 (1998).

5 C. Weltens, J. Menten, M. Feron, E. Bellon, P. Demaerel, F. Maes, W. Van den Bogaert, E. van der Schueren, "Interobserver variations in gross tumor volume delineation of brain tumors on computed tomography and impact of magnetic resonance imaging," Radiotherapy and oncology : journal of the European Society for Therapeutic Radiology and Oncology **60**, 49-59 (2001).

6 J.F. Valley, J. Bernier, P.A. Tercier, A. Fogliata-Cozzi, A. Rosset, G. Garavaglia, R.O. Mirimanoff, "Quality assurance of the EORTC radiotherapy trial 22931 for

head and neck carcinomas: the dummy run," Radiotherapy and oncology : journal of the European Society for Therapeutic Radiology and Oncology **47**, 37-44 (1998).

7 R.C. Krempien, K. Schubert, D. Zierhut, M.C. Steckner, M. Treiber, W. Harms, U. Mende, D. Latz, M. Wannenmacher, F. Wenz, "Open low-field magnetic resonance imaging in radiation therapy treatment planning," International journal of radiation oncology, biology, physics **53**, 1350-1360 (2002).

8 M. Debois, R. Oyen, F. Maes, G. Verswijvel, G. Gatti, H. Bosmans, M. Feron, E. Bellon, G. Kutcher, H. Van Poppel, L. Vanuytsel, "The contribution of magnetic resonance imaging to the three-dimensional treatment planning of localized prostate cancer," International journal of radiation oncology, biology, physics **45**, 857-865 (1999).

9 C. Rasch, R. Keus, F.A. Pameijer, W. Koops, V. de Ru, S. Muller, A. Touw, H. Bartelink, M. van Herk, J.V. Lebesque, "The potential impact of CT-MRI matching on tumor volume delineation in advanced head and neck cancer," International journal of radiation oncology, biology, physics **39**, 841-848 (1997).

10 C. Rasch, R. Steenbakkers, M. van Herk, "Target definition in prostate, head, and neck," Seminars in radiation oncology **15**, 136-145 (2005).

11 M. Jolicoeur, M.L. Racine, I. Trop, L. Hathout, D. Nguyen, T. Derashodian, S. David, "Localization of the surgical bed using supine magnetic resonance and computed tomography scan fusion for planification of breast interstitial brachytherapy," Radiotherapy and oncology : journal of the European Society for Therapeutic Radiology and Oncology **100**, 480-484 (2011).

12 M. Giezen, E. Kouwenhoven, A.N. Scholten, E.G. Coerkamp, M. Heijenbrok, W.P. Jansen, M.E. Mast, A.L. Petoukhova, H. Struikmans, "MRI- versus CT-based volume delineation of lumpectomy cavity in supine position in breast-conserving therapy: an exploratory study," International journal of radiation oncology, biology, physics **82**, 1332-1340 (2012).

13 C. Rasch, I. Barillot, P. Remeijer, A. Touw, M. van Herk, J.V. Lebesque, "Definition of the prostate in CT and MRI: a multi-observer study," International journal of radiation oncology, biology, physics **43**, 57-66 (1999).

14 B. Emami, A. Sethi, G.J. Petruzzelli, "Influence of MRI on target volume delineation and IMRT planning in nasopharyngeal carcinoma," International journal of radiation oncology, biology, physics **57**, 481-488 (2003).

15 N.N. Chung, L.L. Ting, W.C. Hsu, L.T. Lui, P.M. Wang, "Impact of magnetic resonance imaging versus CT on nasopharyngeal carcinoma: primary tumor target delineation for radiotherapy," Head & neck **26**, 241-246 (2004).

16 V.S. Khoo, A.R. Padhani, S.F. Tanner, D.J. Finnigan, M.O. Leach, D.P. Dearnaley, "Comparison of MRI with CT for the radiotherapy planning of prostate cancer: a feasibility study," The British journal of radiology **72**, 590-597 (1999).

17 S. Wachter, N. Wachter-Gerstner, T. Bock, G. Goldner, G. Kovacs, A. Fransson, R. Potter, "Interobserver comparison of CT and MRI-based prostate apex definition. Clinical relevance for conformal radiotherapy treatment planning," Strahlentherapie und Onkologie : Organ der Deutschen Rontgengesellschaft ... [et al] **178**, 263-268 (2002).

[18] M. Urban, H.R. Rosen, N. Holbling, W. Feil, G. Hochwarther, W. Hruby, R. Schiessel, "MR imaging for the preoperative planning of sphincter-saving surgery for tumors of the lower third of the rectum: use of intravenous and endorectal contrast materials," Radiology **214**, 503-508 (2000).

[19] L. Blomqvist, T. Holm, S. Nyren, R. Svanstrom, Y. Ulvskog, L. Iselius, "MR imaging and computed tomography in patients with rectal tumours clinically judged as locally advanced," Clinical radiology **57**, 211-218 (2002).

[20] R.J. Steenbakkers, K.E. Deurloo, P.J. Nowak, J.V. Lebesque, M. van Herk, C.R. Rasch, "Reduction of dose delivered to the rectum and bulb of the penis using MRI delineation for radiotherapy of the prostate," International journal of radiation oncology, biology, physics **57**, 1269-1279 (2003).

[21] R. Potter, J. Dimopoulos, P. Georg, S. Lang, C. Waldhausl, N. Wachter-Gerstner, H. Weitmann, A. Reinthaller, T.H. Knocke, S. Wachter, C. Kirisits, "Clinical impact of MRI assisted dose volume adaptation and dose escalation in brachytherapy of locally advanced cervix cancer," Radiotherapy and oncology : journal of the European Society for Therapeutic Radiology and Oncology **83**, 148-155 (2007).

[22] M. van Herk, H.M. Kooy, "Automatic three-dimensional correlation of CT-CT, CT-MRI, and CT-SPECT using chamfer matching," Med Phys **21**, 1163-1178 (1994).

[23] K. Ulin, M.M. Urie, J.M. Cherlow, "Results of a multi-institutional benchmark test for cranial CT/MR image registration," International journal of radiation oncology, biology, physics **77**, 1584-1589 (2010).

[24] P.L. Roberson, P.W. McLaughlin, V. Narayana, S. Troyer, G.V. Hixson, M.L. Kessler, "Use and uncertainties of mutual information for computed tomography/ magnetic resonance (CT/MR) registration post permanent implant of the prostate," Med Phys **32**, 473-482 (2005).

[25] T. Nyholm, M. Nyberg, M.G. Karlsson, M. Karlsson, "Systematisation of spatial uncertainties for comparison between a MR and a CT-based radiotherapy workflow for prostate treatments," Radiat Oncol **4**, 54 (2009).

[26] D.F. Dubois, W.S. Bice, Jr., B.R. Prestige, "CT and MRI derived source localization error in a custom prostate phantom using automated image coregistration," Med Phys **28**, 2280-2284 (2001).

[27] M. van Herk, "Errors and margins in radiotherapy," Seminars in radiation oncology **14**, 52-64 (2004).

[28] C.K. Glide-Hurst, N. Wen, D. Hearshen, J. Kim, M. Pantelic, B. Zhao, T. Mancell, K. Levin, B. Movsas, I.J. Chetty, M.S. Siddiqui, "Initial clinical experience with a radiation oncology dedicated open 1.0T MR-simulation," Journal of applied clinical medical physics / American College of Medical Physics **16**, 5201 (2015).

[29] V.S. Khoo, D.L. Joon, "New developments in MRI for target volume delineation in radiotherapy," The British journal of radiology **79 Spec No 1**, S2-15 (2006).

[30] E.S. Paulson, B. Erickson, C. Schultz, X. Allen Li, "Comprehensive MRI simulation methodology using a dedicated MRI scanner in radiation oncology for external beam radiation treatment planning," Med Phys **42**, 28 (2015).

[31] K.P. McGee, Y. Hu, E. Tryggestad, D. Brinkmann, B. Witte, K. Welker, A. Panda, M. Haddock, M.A. Bernstein, "MRI in radiation oncology: Underserved needs,"

Magnetic resonance in medicine : official journal of the Society of Magnetic Resonance in Medicine / Society of Magnetic Resonance in Medicine **75**, 11-14 (2016).

[32] M. Kapanen, J. Collan, A. Beule, T. Seppala, K. Saarilahti, M. Tenhunen, "Commissioning of MRI-only based treatment planning procedure for external beam radiotherapy of prostate," Magnetic resonance in medicine : official journal of the Society of Magnetic Resonance in Medicine / Society of Magnetic Resonance in Medicine **70**, 127-135 (2013).

[33] S.H. Hsu, Y. Cao, K. Huang, M. Feng, J.M. Balter, "Investigation of a method for generating synthetic CT models from MRI scans of the head and neck for radiation therapy," Physics in medicine and biology **58**, 8419-8435 (2013).

[34] S.H. Hsu, Y. Cao, T.S. Lawrence, C. Tsien, M. Feng, D.M. Grodzki, J.M. Balter, "Quantitative characterizations of ultrashort echo (UTE) images for supporting air-bone separation in the head," Physics in medicine and biology **60**, 2869-2880 (2015).

[35] J.A. Dowling, J. Lambert, J. Parker, O. Salvado, J. Fripp, A. Capp, C. Wratten, J.W. Denham, P.B. Greer, "An atlas-based electron density mapping method for magnetic resonance imaging (MRI)-alone treatment planning and adaptive MRI-based prostate radiation therapy," International journal of radiation oncology, biology, physics **83**, e5-11 (2012).

[36] J. Lambert, P.B. Greer, F. Menk, J. Patterson, J. Parker, K. Dahl, S. Gupta, A. Capp, C. Wratten, C. Tang, M. Kumar, J. Dowling, S. Hauville, C. Hughes, K. Fisher, P. Lau, J.W. Denham, O. Salvado, "MRI-guided prostate radiation

therapy planning: Investigation of dosimetric accuracy of MRI-based dose planning," Radiotherapy and oncology : journal of the European Society for Therapeutic Radiology and Oncology **98**, 330-334 (2011).

37 D. Rivest-Henault, N. Dowson, P.B. Greer, J. Fripp, J.A. Dowling, "Robust inverse-consistent affine CT-MR registration in MRI-assisted and MRI-alone prostate radiation therapy," Medical image analysis **23**, 56-69 (2015).

38 A.W. Beavis, P. Gibbs, R.A. Dealey, V.J. Whitton, "Radiotherapy treatment planning of brain tumours using MRI alone," The British journal of radiology **71**, 544-548 (1998).

39 Y.K. Lee, M. Bollet, G. Charles-Edwards, M.A. Flower, M.O. Leach, H. McNair, E. Moore, C. Rowbottom, S. Webb, "Radiotherapy treatment planning of prostate cancer using magnetic resonance imaging alone," Radiotherapy and oncology : journal of the European Society for Therapeutic Radiology and Oncology **66**, 203-216 (2003).

40 J.H. Jonsson, M.G. Karlsson, M. Karlsson, T. Nyholm, "Treatment planning using MRI data: an analysis of the dose calculation accuracy for different treatment regions," Radiat Oncol **5**, 62 (2010).

41 B. Petersch, J. Bogner, A. Fransson, T. Lorang, R. Potter, "Effects of geometric distortion in 0.2T MRI on radiotherapy treatment planning of prostate cancer," Radiotherapy and oncology : journal of the European Society for Therapeutic Radiology and Oncology **71**, 55-64 (2004).

42 A.S. Maria, S.P. Geoffrey, "Radiotherapy planning using MRI," Physics in medicine and biology **60**, R323 (2015).

[43] L. Chen, R.A. Price, Jr., T.B. Nguyen, L. Wang, J.S. Li, L. Qin, M. Ding, E. Palacio, C.M. Ma, A. Pollack, "Dosimetric evaluation of MRI-based treatment planning for prostate cancer," Physics in medicine and biology **49**, 5157-5170 (2004).

[44] H. Chang, J.M. Fitzpatrick, "A technique for accurate magnetic resonance imaging in the presence of field inhomogeneities," IEEE transactions on medical imaging **11**, 319-329 (1992).

[45] A. Janke, H. Zhao, G.J. Cowin, G.J. Galloway, D.M. Doddrell, "Use of spherical harmonic deconvolution methods to compensate for nonlinear gradient effects on MRI images," Magnetic Resonance in Medicine **52**, 115-122 (2004).

[46] L.N. Baldwin, K. Wachowicz, S.D. Thomas, R. Rivest, B.G. Fallone, "Characterization, prediction, and correction of geometric distortion in 3 T MR images," Med Phys **34**, 388-399 (2007).

[47] S.J. Doran, L. Charles-Edwards, S.A. Reinsberg, M.O. Leach, "A complete distortion correction for MR images: I. Gradient warp correction," Physics in medicine and biology **50**, 1343-1361 (2005).

[48] S.A. Reinsberg, S.J. Doran, E.M. Charles-Edwards, M.O. Leach, "A complete distortion correction for MR images: II. Rectification of static-field inhomogeneities by similarity-based profile mapping," Physics in medicine and biology **50**, 2651-2661 (2005).

[49] D. Wang, W. Strugnell, G. Cowin, D.M. Doddrell, R. Slaughter, "Geometric distortion in clinical MRI systems Part I: evaluation using a 3D phantom," Magnetic resonance imaging **22**, 1211-1221 (2004).

[50] S.F. Tanner, D.J. Finnigan, V.S. Khoo, P. Mayles, D.P. Dearnaley, M.O. Leach, "Radiotherapy planning of the pelvis using distortion corrected MR images: the removal of system distortions," Physics in medicine and biology **45**, 2117-2132 (2000).

[51] M.M. Breeuwer, M. Holden, W. Zylka, 2001 (unpublished).

[52] K.C. Huang, Y. Cao, U. Baharom, J.M. Balter, "Phantom-based characterization of distortion on a magnetic resonance imaging simulator for radiation oncology," Physics in medicine and biology **61**, 774-790 (2016).

[53] J. Kim, C. Glide-Hurst, A. Doemer, N. Wen, B. Movsas, I.J. Chetty, "Implementation of a Novel Algorithm For Generating Synthetic CT Images From Magnetic Resonance Imaging Data Sets for Prostate Cancer Radiation Therapy," International journal of radiation oncology, biology, physics **91**, 39-47 (2015).

[54] W. Zheng, J.P. Kim, M. Kadbi, B. Movsas, I.J. Chetty, C.K. Glide-Hurst, "Magnetic Resonance-Based Automatic Air Segmentation for Generation of Synthetic Computed Tomography Scans in the Head Region," International journal of radiation oncology, biology, physics **93**, 497-506 (2015).

[55] D. Andreasen, K. Van Leemput, R.H. Hansen, J.A. Andersen, J.M. Edmund, "Patch-based generation of a pseudo CT from conventional MRI sequences for MRI-only radiotherapy of the brain," Med Phys **42**, 1596-1605 (2015).

[56] A. Johansson, M. Karlsson, T. Nyholm, "CT substitute derived from MRI sequences with ultrashort echo time," Med Phys **38**, 2708-2714 (2011).

[57] J. Korhonen, M. Kapanen, J. Keyrilainen, T. Seppala, M. Tenhunen, "A dual model HU conversion from MRI intensity values within and outside of bone

segment for MRI-based radiotherapy treatment planning of prostate cancer," Med Phys **41**, 011704 (2014).

58 J. Sjolund, D. Forsberg, M. Andersson, H. Knutsson, "Generating patient specific pseudo-CT of the head from MR using atlas-based regression," Physics in medicine and biology **60**, 825-839 (2015).

59 Y. Yang, M. Cao, T. Kaprealian, K. Sheng, Y. Gao, F. Han, C. Gomez, A. Santhanam, S. Tenn, N. Agazaryan, D.A. Low, P. Hu, "Accuracy of UTE-MRI-based patient setup for brain cancer radiation therapy," Medical Physics **43**, 262-267 (2016).

60 J. Kim, K. Garbarino, L. Schultz, K. Levin, B. Movsas, M.S. Siddiqui, I.J. Chetty, C. Glide-Hurst, "Dosimetric evaluation of synthetic CT relative to bulk density assignment-based magnetic resonance-only approaches for prostate radiotherapy," Radiat Oncol **10**, 239 (2015).

61 A. Fedorov, R. Beichel, J. Kalpathy-Cramer, J. Finet, J.C. Fillion-Robin, S. Pujol, C. Bauer, D. Jennings, F. Fennessy, M. Sonka, J. Buatti, S. Aylward, J.V. Miller, S. Pieper, R. Kikinis, "3D Slicer as an image computing platform for the Quantitative Imaging Network," Magnetic resonance imaging **30**, 1323-1341 (2012).

62 R.G. Price, M. Kadbi, J. Kim, J. Balter, I.J. Chetty, C.K. Glide-Hurst, "Technical Note: Characterization and correction of gradient nonlinearity induced distortion on a 1.0 T open bore MR-SIM," Med Phys **42**, 5955 (2015).

63 A. Walker, G. Liney, P. Metcalfe, L. Holloway, "MRI distortion: considerations for MRI based radiotherapy treatment planning," Australasian physical & engineering

sciences in medicine / supported by the Australasian College of Physical Scientists in Medicine and the Australasian Association of Physical Sciences in Medicine **37**, 103-113 (2014).

64 T. Stanescu, K. Wachowicz, D.A. Jaffray, "Characterization of tissue magnetic susceptibility-induced distortions for MRIgRT," Med Phys **39**, 7185-7193 (2012).

65 L.N. Baldwin, K. Wachowicz, B.G. Fallone, "A two-step scheme for distortion rectification of magnetic resonance images," Med Phys **36**, 3917-3926 (2009).

66 C.J. Bakker, M.A. Moerland, R. Bhagwandien, R. Beersma, "Analysis of machine-dependent and object-induced geometric distortion in 2DFT MR imaging," Magnetic resonance imaging **10**, 597-608 (1992).

67 C. Hong, D.H. Lee, B.S. Han, "Characteristics of geometric distortion correction with increasing field-of-view in open-configuration MRI," Magnetic resonance imaging **32**, 786-790 (2014).

68 D. Wang, Z. Yang, "A detailed study on the use of polynomial functions for modeling geometric distortion in magnetic resonance imaging," Med Phys **35**, 908-916 (2008).

69 D. Mah, M. Steckner, E. Palacio, R. Mitra, T. Richardson, G.E. Hanks, "Characteristics and quality assurance of a dedicated open 0.23 T MRI for radiation therapy simulation," Med Phys **29**, 2541-2547 (2002).

70 C.D. Fryar, Q. Gu, C.L. Ogden, "Anthropometric reference data for children and adults: United States, 2007-2010," Vital and health statistics. Series 11, Data from the national health survey, 1-48 (2012).

71 H. Gray, W.H. Lewis, *Anatomy of the human body*, 20th ed. (Lea & Febiger, Philadelphia and New York,, 1918).

72 W. Platzer, *Color atlas of human anatomy. Volume 1, Locomotor system*, 6th rev. and enlarged ed. (Thieme, Stuttgart ; New York, 2009).

73 A.H. Buck, T.L. Stedman, *A reference handbook of the medical sciences embracing the entire range of scientific and practical medicine and allied science*, new ed. (W. Wood and company, New York, 1900).

74 A. Fransson, P. Andreo, R. Potter, "Aspects of MR image distortions in radiotherapy treatment planning," Strahlentherapie und Onkologie : Organ der Deutschen Rontgengesellschaft ... [et al] **177**, 59-73 (2001).

75 K. Wachowicz, T. Stanescu, S.D. Thomas, B.G. Fallone, "Implications of tissue magnetic susceptibility-related distortion on the rotating magnet in an MR-linac design," Med Phys **37**, 1714-1721 (2010).

76 P. Jezzard, R.S. Balaban, "Correction for geometric distortion in echo planar images from B0 field variations," Magnetic resonance in medicine : official journal of the Society of Magnetic Resonance in Medicine / Society of Magnetic Resonance in Medicine **34**, 65-73 (1995).

77 D. Wang, D.M. Doddrell, G. Cowin, "A novel phantom and method for comprehensive 3-dimensional measurement and correction of geometric distortion in magnetic resonance imaging," Magnetic resonance imaging **22**, 529-542 (2004).

78 K. Hwang, F. Illerstam, T. Torfeh, J. Maier, S. Shave, M. Hoang, "SU-E-J-146: Spatial Accuracy QA of An MR System," Medical Physics **41**, 189-190 (2014).

79 A. Mix, A. Giacomin, "Standardized Polymer Durometry," 1-10 (2011).

80 W. Schroeder, K. Martin, B. Lorensen, *The visualization toolkit*, 2nd ed. (Prentice Hall PTR, Upper Saddle River, NJ, 1998).

81 https://www.qt.io/.

82 T.S. Yoo, M.J. Ackerman, W.E. Lorensen, W. Schroeder, V. Chalana, S. Aylward, D. Metaxas, R. Whitaker, "Engineering and algorithm design for an image processing Api: a technical report on ITK--the Insight Toolkit," Stud Health Technol Inform **85**, 586-592 (2002).

83 T. Torfeh, R. Hammoud, M. McGarry, N. Al-Hammadi, G. Perkins, "Development and validation of a novel large field of view phantom and a software module for the quality assurance of geometric distortion in magnetic resonance imaging," Magnetic Resonance Imaging **33**, 939-949 (2015).

84 T. Torfeh, R. Hammoud, G. Perkins, M. McGarry, S. Aouadi, A. Celik, K.P. Hwang, J. Stancanello, P. Petric, N. Al-Hammadi, "Characterization of 3D geometric distortion of magnetic resonance imaging scanners commissioned for radiation therapy planning," Magnetic resonance imaging **34**, 645-653 (2016).

85 C. Pinter, A. Lasso, A. Wang, D. Jaffray, G. Fichtinger, "SlicerRT: radiation therapy research toolkit for 3D Slicer," Med Phys **39**, 6332-6338 (2012).

86 R.G. Price, J.P. Kim, W. Zheng, I.J. Chetty, C. Glide-Hurst, "Image Guided Radiation Therapy Using Synthetic Computed Tomography Images in Brain Cancer," International journal of radiation oncology, biology, physics2016).

87 D.P. Gierga, G.T. Chen, J.H. Kung, M. Betke, J. Lombardi, C.G. Willett, "Quantification of respiration-induced abdominal tumor motion and its impact on

IMRT dose distributions," International journal of radiation oncology, biology, physics **58**, 1584-1595 (2004).

88 A. Pollack, G.K. Zagars, G. Starkschall, J.A. Antolak, J.J. Lee, E. Huang, A.C. von Eschenbach, D.A. Kuban, I. Rosen, "Prostate cancer radiation dose response: results of the M. D. Anderson phase III randomized trial," International journal of radiation oncology, biology, physics **53**, 1097-1105 (2002).

89 B. Chauvet, G. de Rauglaudre, L. Mineur, M. Alfonsi, F. Reboul, "[Dose-response relationship in radiotherapy: an evidence?]," Cancer radiotherapie : journal de la Societe francaise de radiotherapie oncologique **7 Suppl 1**, 8s-14s (2003).

90 E.H. Pow, D.L. Kwong, A.S. McMillan, M.C. Wong, J.S. Sham, L.H. Leung, W.K. Leung, "Xerostomia and quality of life after intensity-modulated radiotherapy vs. conventional radiotherapy for early-stage nasopharyngeal carcinoma: initial report on a randomized controlled clinical trial," International journal of radiation oncology, biology, physics **66**, 981-991 (2006).

91 T.R. Mackie, J. Kapatoes, K. Ruchala, W. Lu, C. Wu, G. Olivera, L. Forrest, W. Tome, J. Welsh, R. Jeraj, P. Harari, P. Reckwerdt, B. Paliwal, M. Ritter, H. Keller, J. Fowler, M. Mehta, "Image guidance for precise conformal radiotherapy," International journal of radiation oncology, biology, physics **56**, 89-105 (2003).

92 L. Potters, M. Steinberg, C. Rose, R. Timmerman, S. Ryu, J.M. Hevezi, J. Welsh, M. Mehta, D.A. Larson, N.A. Janjan, R. American Society for Therapeutic, Oncology, R. American College of, "American Society for Therapeutic Radiology and Oncology and American College of Radiology practice guideline for the

performance of stereotactic body radiation therapy," International journal of radiation oncology, biology, physics **60**, 1026-1032 (2004).

93 J. Uh, T.E. Merchant, Y. Li, X. Li, C. Hua, "MRI-based treatment planning with pseudo CT generated through atlas registration," Med Phys **41**, 051711 (2014).

94 J. Korhonen, M. Kapanen, J.J. Sonke, L. Wee, E. Salli, J. Keyrilainen, T. Seppala, M. Tenhunen, "Feasibility of MRI-based reference images for image-guided radiotherapy of the pelvis with either cone-beam computed tomography or planar localization images," Acta oncologica **54**, 889-895 (2015).

95 J.M. Edmund, D. Andreasen, F. Mahmood, K. Van Leemput, "Cone beam computed tomography guided treatment delivery and planning verification for magnetic resonance imaging only radiotherapy of the brain," Acta oncologica **54**, 1496-1500 (2015).

96 H. Wang, J. Balter, Y. Cao, "Patient-induced susceptibility effect on geometric distortion of clinical brain MRI for radiation treatment planning on a 3T scanner," Physics in medicine and biology **58**, 465-477 (2013).

97 M. Jenkinson, "A fast, automated, n-dimensional phase unwrapping algorithm," Magn. Reson. Med. **49**, 193–197 (2003).

98 S.M. Smith, M. Jenkinson, M.W. Woolrich, C.F. Beckmann, T. Behrens, H. Johansen-Berg, P.R. Bannister, M. De Luca, I. Drobnjak, D.E. Flitney, R. Niazy, J. Saunders, J. Vickers, Y. Zhang, N. De Stefano, J.M. Brady, P.M. Matthews, "Advances in functional and structural MR image analysis and implementation as FSL," NeuroImage **23** 208-219 (2004).

99 M.W. Woolrich, S. Jbabdi, B. Patenaude, M. Chappell, S. Makni, T. Behrens, C. Beckmann, M. Jenkinson, S.M. Smith, "Bayesian analysis of neuroimaging data in FSL," NeuroImage **45**, S173-186 (2009).

100 C.D. Hines, H. Yu, A. Shimakawa, C.A. McKenzie, J.H. Brittain, S.B. Reeder, "T1 independent, T2* corrected MRI with accurate spectral modeling for quantification of fat: validation in a fat-water-SPIO phantom," J Magn Reson Imaging **30**, 1215–1222 (2009).

101 D.H. Kim, N. Choi, S.M. Gho, J. Shin, C. Liu, "Simultaneous imaging of in vivo conductivity and susceptibility," Magnetic resonance in medicine : official journal of the Society of Magnetic Resonance in Medicine / Society of Magnetic Resonance in Medicine **71**, 1140-1150 (2014).

102 A.P. Dempster, N.M. Laird, D.B. Rubin, "Maximum likelihood from incomplete data via the EM algorithm," J. R. Statist. Soc. Series B **39**, 1-38 (1977).

103 S. Klein, M. Staring, K. Murphy, M. Viergever, J. Pluim, "Elastix: A toolbox for intensity based medical image registration," IEEE Trans. Med. Imaging **29**, 196-205 (2010).

104 S. Klein, J.W. Pluim, M. Staring, M. Viergever, "Adaptive Stochastic Gradient Descent Optimisation for Image Registration," International Journal of Computer Vision **81**, 227-239 (2009).

105 M. van Herk, P. Remeijer, J.V. Lebesque, "Inclusion of geometric uncertainties in treatment plan evaluation," International journal of radiation oncology, biology, physics **52**, 1407-1422 (2002).

106 H. Yu, C. Caldwell, J. Balogh, K. Mah, "Toward magnetic resonance-only simulation: segmentation of bone in MR for radiation therapy verification of the head," International journal of radiation oncology, biology, physics **89**, 649-657 (2014).

107 J.H. Jonsson, A. Johansson, K. Soderstrom, T. Asklund, T. Nyholm, "Treatment planning of intracranial targets on MRI derived substitute CT data," Radiotherapy and oncology : journal of the European Society for Therapeutic Radiology and Oncology **108**, 118-122 (2013).

108 T. Fox, C. Huntzinger, P. Johnstone, T. Ogunleye, E. Elder, "Performance evaluation of an automated image registration algorithm using an integrated kilovoltage imaging and guidance system," Journal of applied clinical medical physics / American College of Medical Physics **7**, 97-104 (2006).

109 S. Arumugam, M.G. Jameson, A. Xing, L. Holloway, "An accuracy assessment of different rigid body image registration methods and robotic couch positional corrections using a novel phantom," Med Phys **40**, 031701 (2013).

110 S.D. Sharma, P. Dongre, V. Mhatre, M. Heigrujam, "Evaluation of automated image registration algorithm for image-guided radiotherapy (IGRT)," Australasian physical & engineering sciences in medicine / supported by the Australasian College of Physical Scientists in Medicine and the Australasian Association of Physical Sciences in Medicine **35**, 311-319 (2012).

111 F.-F. Yin, Q. Gao, H. Xie, D.F. Nelson, Y. Yu, W.E. Kwok, S. Totterman, M.C. Schell, P. Rubin, "MR image-guided portal verification for brain treatment field,"

International Journal of Radiation Oncology* Biology* Physics **40**, 703-711 (1998).

112 M. Mehta, Gondi, V., Mahajan, A., Shih, H., et al, "Randomized Phase II Trial of Hypofractionated Dose-Escalated Photon IMRT or Proton Beam Therapy Versus Conventional Photon Irradiation with Concomitant and Adjuvant Temozolomide in Patients with Newly Diagnised Glioblastoma," (Radiation Therapy Oncology Group (RTOG).).

113 M.E. Korsholm, L.W. Waring, J.M. Edmund, "A criterion for the reliable use of MRI-only radiotherapy," Radiat Oncol **9**, 16 (2014).

114 J. Sun, J. Dowling, P. Pichler, F. Menk, D. Rivest-Henault, J. Lambert, J. Parker, J. Arm, L. Best, J. Martin, J.W. Denham, P.B. Greer, "MRI simulation: end-to-end testing for prostate radiation therapy using geometric pelvic MRI phantoms," Physics in medicine and biology **60**, 3097-3109 (2015).

115 I. Barillot, A. Reynaud-Bougnoux, "The use of MRI in planning radiotherapy for gynaecological tumours," Cancer Imaging **6**, 100-106 (2006).

116 M. Pech, K. Mohnike, G. Wieners, E. Bialek, O. Dudeck, M. Seidensticker, N. Peters, P. Wust, G. Gademann, J. Ricke, "Radiotherapy of liver metastases. Comparison of target volumes and dose-volume histograms employing CT- or MRI-based treatment planning," Strahlentherapie und Onkologie : Organ der Deutschen Rontgengesellschaft ... [et al] **184**, 256-261 (2008).

117 W.C. Liu, M. Schulder, V. Narra, A.J. Kalnin, C. Cathcart, A. Jacobs, G. Lange, A.I. Holodny, "Functional magnetic resonance imaging aided radiation treatment planning," Med Phys **27**, 1563-1572 (2000).

[118] J. Van Dyk, *The modern technology of radiation oncology : a compendium for medical physicists and radiation oncologists*. (Medical Physics Pub., Madison, Wis., 1999).

[119] E.E. Klein, J. Hanley, J. Bayouth, F.F. Yin, W. Simon, S. Dresser, C. Serago, F. Aguirre, L. Ma, B. Arjomandy, C. Liu, C. Sandin, T. Holmes, A.A.o.P.i.M. Task Group, "Task Group 142 report: quality assurance of medical accelerators," Med Phys **36**, 4197-4212 (2009).

[120] A.K. Singh, P. Guion, N. Sears-Crouse, K. Ullman, S. Smith, P.S. Albert, G. Fichtinger, P.L. Choyke, S. Xu, J. Kruecker, B.J. Wood, A. Krieger, H. Ning, "Simultaneous integrated boost of biopsy proven, MRI defined dominant intra-prostatic lesions to 95 Gray with IMRT: early results of a phase I NCI study," Radiat Oncol **2**, 36 (2007).

[121] D.A. Hoover, D.P. Capaldi, K. Sheikh, D.A. Palma, G.B. Rodrigues, A.R. Dar, E. Yu, B. Dingle, M. Landis, W. Kocha, M. Sanatani, M. Vincent, J. Younus, S. Kuruvilla, S. Gaede, G. Parraga, B.P. Yaremko, "Functional lung avoidance for individualized radiotherapy (FLAIR): study protocol for a randomized, double-blind clinical trial," BMC Cancer **14**, 934 (2014).

[122] S. Mutic, J.F. Dempsey, "The ViewRay system: magnetic resonance-guided and controlled radiotherapy," Seminars in radiation oncology **24**, 196-199 (2014).

[123] B.W. Raaymakers, J.J. Lagendijk, J. Overweg, J.G. Kok, A.J. Raaijmakers, E.M. Kerkhof, R.W. van der Put, I. Meijsing, S.P. Crijns, F. Benedosso, M. van Vulpen, C.H. de Graaff, J. Allen, K.J. Brown, "Integrating a 1.5 T MRI scanner with a 6

MV accelerator: proof of concept," Physics in medicine and biology **54**, N229-237 (2009).

[124] P.J. Keall, M. Barton, S. Crozier, i.c.f.I.I.I.C.C.C.L.H.S.U.U.o.N.Q.S.W.S. Australian Mri-Linac Program, Wollongong, "The Australian magnetic resonance imaging-linac program," Seminars in radiation oncology **24**, 203-206 (2014).

[125] B.G. Fallone, "The rotating biplanar linac-magnetic resonance imaging system," Seminars in radiation oncology **24**, 200-202 (2014).

ABSTRACT

TOWARD MAGNETIC RESONANCE ONLY TREATMENT PLANNING: DISTORTION MITIGATION AND IMAGE-GUIDED RADIATION THERAPY VALIDATION

by

RYAN GLEN PRICE

August 2016

Advisor: Dr. Carri K. Glide-Hurst

Major: Medical Physics

Degree: Doctor of Philosophy

While MR-only treatment planning has shown promise, there are still several well-known challenges that are currently limiting widespread clinical implementation. Firstly, MR images are affected by both patient-induced and system-level geometric distortions that can significantly degrade treatment planning accuracy. . In addition, the availability of comprehensive distortion analysis software is currently limited. Also while many groups have been working toward a synthetic CT solution, further study is needed on the implementation of synCTs as the reference datasets for linac-based image-guided radiation therapy (IGRT) to help determine their robustness in an MR-only workflow.

A 36×43×2 cm^3 phantom with 255 known landmarks (~1 mm^3) was scanned using 1.0T high-field open MR-SIM at isocenter in the transverse, sagittal, and coronal axes, and a 465x350x168mm 3D phantom was scanned by stepping in the superior-inferior direction in 3 overlapping positions to achieve a total 465x350x400mm sampled FOV yielding >13,800 landmarks(3D Gradient-Echo, TE/TR/α = 5.54 ms/30 ms/28°, voxel size =1×1×2mm^3). A binary template (reference) was generated from a phantom

schematic. An automated program converted MR images to binary via masking, thresholding, and testing for connectivity to identify landmarks. Distortion maps were generated by centroid mapping. Images were corrected via warping with inverse distortion maps, and temporal stability was assessed.

To determine candidate materials for phantom and software development, 1.0 T MR and CT images were acquired of twelve urethane foam samples of various densities and strengths. Samples were precision machined to accommodate 6 mm diameter paintballs used as landmarks. Final material candidates were selected by balancing strength, machinability, weight, and cost. Bore sizes and minimum aperture width resulting from couch position were tabulated from the literature (14 systems, 5 vendors). Bore geometry and couch position were simulated using MATLAB to generate machine-specific models to optimize the phantom build. Previously developed software for distortion characterization was modified for several magnet geometries (1.0 T, 1.5 T, 3.0 T), compared against previously published 1.0 T results, and integrated into the 3DSlicer application platform.

To evaluate the performance of synthetic CTs in an image guided workflow, magnetic resonance simulation and CT simulation images were acquired of an anthropomorphic skull phantom and 12 patient brain cancer cases. SynCTs were generated using fluid attenuation inversion recovery, ultrashort echo time, and Dixon data sets through a voxel-based weighted summation of 5 tissue classifications. The DRRs were generated from the phantom synCT, and geometric fidelity was assessed relative to CT-generated DRRs through bounding box and landmark analysis. An offline retrospective analysis was conducted to register cone beam CTs to synCTs and CTs

using automated rigid registration in the treatment planning system. Planar MV and KV images were rigidly registered to synCT and CT DRRs using an in-house script. Planar and volumetric registration reproducibility was assessed and margin differences were characterized by the van Herk formalism.

Over the sampled FOV, non-negligible residual gradient distortions existed as close as 9.5 cm from isocenter, with a maximum distortion of 7.4mm as close as 23 cm from isocenter. Over 6 months, average gradient distortions were -0.07±1.10 mm and 0.10±1.10 mm in the x and y-directions for the transverse plane, 0.03±0.64 and -0.09±0.70 mm in the sagittal plane, and 0.4±1.16 and 0.04±0.40 mm in the coronal plane. After implementing 3D correction maps, distortions were reduced to < 1 pixel width (1mm) for all voxels up to 25 cm from magnet isocenter.

All foam samples provided sufficient MR image contrast with paintball landmarks. Urethane foam (compressive strength ~1000psi, density ~20lb/ft^3) was selected for its accurate machinability and weight characteristics. For smaller bores, a phantom version with the following parameters was used: 15 foam plates, 55×55×37.5 cm^3 (L×W×H), 5,082 landmarks, and weight ~30 kg. To accommodate >70 cm wide bores, an extended build used 20 plates spanning 55×55×50 cm^3 with 7,497 landmarks and weight ~44 kg. Distortion characterization software was implemented as an external module into 3DSlicer's plugin framework and results agreed with the literature.

Bounding box and landmark analysis of phantom synCT DRRs were within 1 mm of CT DRRs. Absolute planar registration shift differences ranged from 0.0 to 0.7 mm for phantom DRRs on all treatment platforms and from 0.0 to 0.4 mm for volumetric registrations. For patient planar registrations, the mean shift differences were 0.4±0.5

mm (range, 0.6 to 1.6 mm), 0.0±0.5 mm (range, 0.9 to 1.2 mm), and 0.1±0.3 mm (range, 0.7 to 0.6 mm) for the superior-inferior (S-I), left-right (L-R), and anterior-posterior (A-P) axes, respectively. The mean shift differences in volumetric registrations were 0.6±0.4 mm (range, 0.2 to 1.6 mm), 0.2±0.4 mm (range, 0.3 to 1.2 mm), and 0.2±0.3 mm (range, 0.2 to 1.2 mm) for the S-I, L-R, and A-P axes, respectively. The CT-SIM and synCT derived margins were <0.3mm different.

This work has characterized the inaccuracies related to GNL distortion for a previously uncharacterized MR-SIM system at large FOVs, and established that while distortions are still non-negligible after current vendor corrections are applied, simple post-processing methods can be used to further reduce these distortions to less than 1mm for the entire field of view. Additionally, it was important to not only establish effective corrections, but to establish the previously uncharacterized temporal stability of these corrections. This work also developed methods to improve the accessibility of these distortion characterizations and corrections. We first tested the application of a more readily available 2D phantom as a surrogate for 3D distortion characterization by stepping the table with an integrated batch script file. Later we developed and constructed a large modular distortion phantom using easily obtainable materials, and showed and constructed a large modular distortion phantom using easily obtainable materials, and used it to characterize the distortion on several widely available MR systems. To accompany this phantom, open source software was also developed for easy characterization of system-dependent distortions. Finally, while the dosimetric equivalence of synCT with CT has been well established, it was necessary to characterize any differences that may exist between synCT and CT in an IGRT setting.

This work has helped to establish the geometric equivalence of these two modalities, with some caveats that have been discussed at length.

AUTOBIOGRAPHICAL STATEMENT
RYAN GLEN PRICE

EDUCATION

2011-2016 Ph.D. Medical Physics, Wayne State University, Detroit, MI
Computer Science Minor

2007-2011 Honors B.S. Physics, University of Utah, Salt Lake City, Utah
Mathematics Minor

CERTIFICATION

2012 American Board of Radiology Part 1

PROFESSIONAL APPOINTMENTS

2013-2016 Graduate Research Assistant, Henry Ford Health System
Department of Radiation Oncology, Detroit, MI

2013-2013 Volunteer Research Assistant, Henry Ford Health System
Department of Radiation Oncology, Detroit, MI

2012-2013 Graduate Teaching Assistant, Wayne State University
Department of Radiation Oncology, Detroit, MI

2009-2012 Research Assistant, University of Utah
Department of Physics and Astronomy, Salt Lake City, Utah

ACADEMIC AND PROFESSIONAL MEMBERSHIPS

2015- American College of Radiology

2013- American Association of Physicists in Medicine, Great Lakes Chapter

2011- American Association of Physicists in Medicine

2008- American Physical Society

AWARDS & COMMITTEE APPOINTMENTS

2016 Runner-up Best Presentation at GLC-AAPM Young Investigator Symposium

2015- AAPM Working Group on Student and Trainee Research: Member

2015 Runner-up Best Presentation at GLC-AAPM Young Investigator Symposium

2014 Runner-up Best Presentation at GLC-AAPM Young Investigator Symposium

2013 Runner-up Best Presentation at GLC-AAPM Young Investigator Symposium

2011 Undergraduate Research Scholar

2011 Service-Learning Scholar

PUBLICATIONS

1. **Price, R.G.**, Kim, J., Zheng, W., Chetty, I.J., Glide-Hurst, C. *"Image-guided Radiation Therapy Using Synthetic CTs in Brain Cancer."* In Print: Int. J. Radiation Oncol. Biol. Phys. (2016)
2. To, D., Kim, J.P., **Price, R.G.**, Chetty, I.J., Glide-Hurst, C. *"Impact of Incorporating Visual Biofeedback in 4DMRI."* Journal of Applied Clinical Medical Physics/American College of Medical Physics **17**, 6017 (2016).
3. **Price, R.G.**, Kadbi, M., Kim, J., Chetty, I.J., and Glide-Hurst, C. *"Technical Note: Characterization and Correction of Gradient Non-Linearity Induced Distortion on a 1.0 Tesla Open Bore MR-SIM."* Med. Phys., 42(10), 5955-5960. (2015)
4. Glide-Hurst, C.K., Shah, M.M., **Price, R.G.**, Liu, C., Kim, J., Mahan, M., Fraser, C., Chetty, I.J., Aref, I., Movsas, B., Walker, E. *"Intrafraction Variability and Deformation Quantification in the Breast."* Int. J. Radiation Oncol. Biol. Phys. 91(3), 604-611. (2015)
5. **Price, R.G.**, Vance, S., Cattaneo II, R., Shultz, L., Elshaikh, M., Chetty, I.J., and Glide-Hurst, C. *"Characterization of a Commercial Hybrid Iterative and Model-Based Reconstruction Algorithm in Radiation Oncology."* Med. Phys. 41, 081907 (13pp.) (2014)